ENERGETIC CAVITATION COLLAPSE

By

Marc Christopher Ramsey

Dissertation

Submitted to the Faculty of the

Graduate School of Vanderbilt University

in partial fulfillment of the requirements

for the degree of

DOCTOR OF PHILOSOPHY

in

Mechanical Engineering

August, 2013

Nashville, Tennessee

Approved:

Professor Robert W. Pitz

Professor Haoxiang Luo

Professor Jon F. Edd

Professor Amrutur V. Anilkumar

Professor M. Shane Hutson

To Jenny, who makes all of this worthwhile.

ACKNOWLEDGEMENTS

This work was made possible by generous financial support from the National Science Foundation Graduate Research Fellowship; the Vanderbilt University Graduate Research Fellowship, Discovery Grant, Dissertation Enhancement Grant, and Travel Grant programs; and by a grant and equipment loan from Sandia National Laboratories made possible by Mike Cuneo, Briggs Atherton and Matthias Geissel. I am also grateful for essential equipment loans from Vanderbilt faculty members John Edd and Jason Valentine.

I would like to thank the members of my committee for their time and advice, contributed freely and without recompense. Haoxiang Luo made a critical contribution of time and expertise in the development of the simulation code. I would especially like to thank my advisor and committee chair, Robert Pitz, for unlimited and unwavering support despite my decision to pursue a high risk project which did not directly contribute to his own research interests.

Most importantly I thank my wife Jenny. She is the light of my life, and it is only by her support that any of this has come to pass. She moved to Albuquerque and again to Nashville as I followed my passion, lived five years on a student stipend, and now lives with the uncertainty of what is to come.

TABLE OF CONTENTS

LIST OF FIGURES

LIST OF ABBREVIATIONS

1D	one dimensional
CW	continuous wave
ECC	energetic cavitation collapse
FWHM	full width at half maximum
ICCD	intensified charge coupled device
ODE	ordinary differential equation
PDE	partial differential equation
PMT	photo-multiplier tube
PZT	piezo-electric element (specifically, $Pb[Zr_xTi_{(1-x)}]O_3$)
RMS	root mean squared
RP	Rayleigh-Plesset
SBSL	single bubble sonoluminescence
STP	standard temperature and pressure

CHAPTER I

INTRODUCTION

Cavitation

Cavitation refers to the formation and collapse of cavities, or bubbles, in a liquid as a result of pressure changes. Cavitation often occurs spontaneously in a liquid volume by convection to a region of low pressure or by acoustic excitation. Cavitation bubbles are generally formed at nucleation sites, which include impurities, particles, or micro-bubbles within the liquid volume or particular geometric irregularities on solid surfaces[1]. The collapse of cavitation bubbles is often violent, producing momentary extremes of pressure and temperature, and emitting shock waves and light[2]. This phenomenon is undesirable and destructive to devices such as pumps, hydrofoils, and propellers. However, these events are put to constructive use in industrial applications such as ultrasonic cleaning and drilling, in medical applications including the destruction of kidney stones by shock wave lithotripsy and the insertion of large molecules into living cells by sonoporation, and in chemical applications including mixing and sonochemistry.

Spherical bubble dynamics

We now follow Brennen[1] for a brief overview of simplified bubble dynamics, though we will depart slightly from his notation to suit our purposes. We assume a spherical bubble with time varying radius $R(t)$ centered on a 1D coordinate system with radial coordinate r. We assume the liquid incompressible and the pressure in the bubble uniform, then solve the Navier-Stokes equations for the liquid with appropriate boundary

conditions at the bubble wall and far-field to arrive at the incompressible Rayleigh-Plesset equation

$$[p_B - p_\infty] = \rho_L \left(R\ddot{R} + \frac{3}{2}\dot{R}^2 \right) + 4\mu \frac{\dot{R}}{R} - \frac{2\sigma}{R} \tag{1}$$

where $p_B(t)$ is the pressure in the bubble, $p_\infty(t)$ is the far-field liquid pressure, ρ_L is the liquid density, μ is the dynamic viscosity of the liquid, σ is the coefficient of surface tension of the liquid, and over-dots indicate differentiation with respect to time.

A cavitation bubble generally contains a mixture of gases, which we here simplify by dividing into two species – vapor and gas. The pressure inside the bubble is

$$p_B = p_V + p_G \tag{2}$$

where p_V is the partial pressure of the vapor and p_G is the partial pressure of the gas.

During all but the fastest bubble dynamics, the vapor freely crosses the bubble wall by evaporation and condensation, and the heat capacity of a thin lamella of liquid surrounding the bubble is large compared to the latent heat of condensation of the entire mass of vapor contained within. As a result, latent thermal effects are negligible and we assume the pressure of the vapor remains a constant function of far-field liquid temperature only, i.e.

$$p_V = p_v(T_\infty) \tag{3}$$

where p_v is the saturated vapor pressure of the liquid at the ambient temperature of the liquid far from the bubble T_∞.

The gas is generally soluble in the liquid but non-condensable. Over long times, the average gas pressure within the bubble will be a function of the concentration of dissolved gas in the liquid by Henry's law,

$$p_G = k_H c_\infty \tag{4}$$

where k_H is Henry's constant and c_∞ is the concentration of gas dissolved in the liquid far from the bubble. However, the time scale of this equilibrium is limited by the diffusion

of the gas in the liquid, which is slow. During a typical bubble oscillation period or a single collapse event, transport of gas across the bubble wall is negligible, and the mass of gas inside the bubble can be considered fixed.

To develop a simple approximation for spherical bubble dynamics, we assume the gas is ideal and follows a polytropic process path, so that its partial pressure is

$$p_G = p_{G0}\left(\frac{R_0}{R}\right)^{3k} \tag{5}$$

where p_{G0} and R_0 are the gas pressure and bubble radius at the initial reference state and k is the polytropic exponent, which may vary from 1 in the isothermal limit to γ, the ratio of specific heats, in the adiabatic limit assuming constant specific heats.

Given an initial condition and a function $p_\infty(t)$, we are now prepared to solve equation (1) for bubble radius evolution $R(t)$. Note that we have made many assumptions which are violated in the final stages of any physical energetic collapse, such as the incompressible liquid and ideal gas assumptions. Nevertheless, this simple theory illustrates the basic energy focusing phenomenon and relevant scaling relations.

Collapse and energy focusing

Energy focusing during cavitation collapse is most concisely illustrated by a simple example. We assume a bubble which is initially at rest at radius $R = R_0$ and contains a small quantity of gas $p_{G0} \ll p_v$ at temperature T_0 is then subjected to a step increase in far-field drive pressure to some large value $p_\infty^* \gg p_v$. Since the pressure inside the bubble remains negligible until it is very small, the total kinetic energy of the collapse will be equal to the work done on the collapsing cavity by the far-field pressure

$$E = \left(\frac{4\pi}{3}\right) R_0^3 p_\infty^* \tag{6}$$

Integrating equation (1) and neglecting small terms, we find that the total collapse time[2] will be

$$t_{TC} = 0.915\sqrt{\frac{\rho_L R_0^2}{p_\infty^*}} \tag{7}$$

and the collapse will come to a halt at stagnation radius, interior pressure and interior temperature[1]

$$R_{stag} = R_0\left(\frac{p_{G0}}{p_\infty^*(k-1)}\right) \tag{8}$$

$$p_{stag} = p_{G0}\left(\frac{p_\infty^*(k-1)}{p_{G0}}\right)^{\frac{k}{k-1}} \tag{9}$$

$$T_{stag} = T_0\left(\frac{p_\infty^*(k-1)}{p_{G0}}\right) \tag{10}$$

If we assume that the gas is air and the collapse is fast compared to thermal diffusion so that the bubble wall is adiabatic, we may estimate that $k \cong 1.4$. We thus observe directly that the stagnation pressure scales with ${p_\infty^*}^{3.5} p_{G0}^{-2.5}$. That is strong scaling, and suggests that extreme pressures might be reached with appropriate initial conditions. As we shall see below, it is not uncommon to observe stagnation pressures of tens of kilobar in a simple event.

To illustrate conceptually the energy focusing phenomenon that occurs here, we consider the flow of energy. The far-field driving pressure does work on the cavity, adding a finite quantity of kinetic energy to the imploding incompressible fluid flow while the pressure of the bubble interior is negligible. The collapse then proceeds unhindered until the pressure of the bubble interior becomes significant. It does not come to a halt until the entire collapse energy has been transferred to the bubble interior by work done on the interior by the bubble wall. So the ultimate energy density is simply the ratio of the collapse energy to the volume of the bubble at stagnation. If the quantity of gas in the bubble is small, then the stagnation radius (and volume) may be very small indeed. Thus, the stagnation pressure (a unit of energy density) may become arbitrarily large.

It should be understood that, in the real case, the liquid is not incompressible. This does limit the energy focusing since a fraction of the collapse energy is converted to enthalpy in the liquid without being deposited in the bubble interior as described in the preceding paragraph.

Single bubble sonoluminescence

The phenomenon of cavitation collapse has been most carefully studied in the context of context of single-bubble sonoluminescence (SBSL)[3–6] in which a bubble is driven to periodic expansion and collapse by an acoustic standing wave. On each collapse, the bubble contents are compressed and heated, emitting light and a shock at stagnation.

A defining characteristic of the SBSL mechanism is that a single bubble oscillates in quasi-equilibrium. This is convenient for experimental observation – the bubble remains stationary for hours, repeatedly collapsing at about 20 kHz, allowing measurements to be integrated over long periods of time. However, this also means that the experimental parameters are coupled in complex ways and have limitations imposed by the equilibrium. For example, the quantity of gas inside the bubble is driven by diffusive equilibrium and equation (4), and is thus coupled to the concentration of gas dissolved in the liquid, Henry's constant for the liquid / gas pair, the ambient temperature, and both the amplitude and frequency of the acoustic wave (which drive the dynamics and average size of the bubble). Outside certain bounds, the bubble will either dissolve completely or grow without bound and become dynamically unstable.

The equilibria and instabilities which govern the SBSL parameter space include diffusive, chemical, harmonic, and shape effects, and are exhaustively itemized by Brenner et. al.[5]. In practical devices, these generally confine SBSL to bubbles with maximum radius of ~50 μm driven by ultrasonic excitation with frequency of ~20 kHz and

amplitude of 1-2 bar, leading to collapse energies of about 50 nJ and stagnation radius of ~1μm. These events generally produce a picosecond[7,8] burst of light and emit a strong shock wave[2,9–14] into the liquid at stagnation.

Theoretical predictions of the conditions produced inside the bubble during these stagnation events vary widely depending on the assumptions made and the physical mechanisms which are modeled. The most significant unknown is whether or not shock waves form in the bubble interior during the stagnation event. A highly cited study by Wu and Roberts[15] and supported by others[16,17] finds that a converging shock wave reflects at the bubble center, generating peak pressures and temperatures above 10 Mbar and 10^7 K in a small central region of the bubble. If this result is physical, it would be extraordinary indeed, since these conditions could initiate nuclear fusion reactions[18] in deuterium. However, other studies[19,20] find that the predicted occurrence of the converging shock is sensitive to the model assumptions and may not occur. In this case, the bubble interior would behave isentropically, resulting in peak pressures and temperatures less than 100 kbar and a few 10^4 K as predicted by equations (9) and (10).

Note that the dynamics of the shock wave which forms in the liquid outside the bubble are largely insensitive to the dynamics inside the bubble. Regardless of whether the bubble interior develops shocks or remains isentropic, the stagnation event is very short compared to acoustic times in the liquid at distances on the order of the stagnation radius. Thus, the liquid behaves essentially the same at distances beyond a few stagnation radii and cannot be used to infer the interior dynamics.

Experimental measurements of the stagnation temperature and pressure during SBSL are difficult. The picosecond time scales challenge the fastest detectors and the sub-micron length scales are below the practical imaging resolution at visible wavelengths. As a result, the stagnation conditions are generally inferred from time-

integrated emission spectra and from observation of the shock wave emitted in the liquid. Measurements of temperature[21–25] generally lie in the vicinity of 10^4 K, with several studies suggesting evidence for a hot bubble core[26–29] at up to a few 10^5 K. Measurements of pressure[13,14,25] are generally in the range of 1-60 kbar. Taken as a whole, these measurements are generally inconclusive as to whether or not shock waves form inside the collapsing bubble, and this is a topic of debate in the literature.

SBSL variants and upscaled cavitation collapses

Many attempts have been made to avoid the parameter space limitations imposed by SBSL in order to produce larger or more energetic collapses. These generally fall into two classes, which I will refer to as SBSL variants and single-shot methods, respectively.

SBSL variants are all based on an oscillating bubble and are subject to the same equilibria as SBSL, but with modified geometry, drive frequency, or acoustic waveform, or with the addition of transient perturbations designed to intensify one particular collapse cycle. Thomas et. al.[30,31] used an array of 8 piezo transducers to add a positive pressure spike to the sinusoidal drive waveform of an SBSL bubble, and reported a “brightness gain”. Several groups[32–36] used multiple acoustic harmonics to modify the acoustic waveform and reported increased light emission. Several groups[37–39] reported stable oscillating bubbles in perodically accelerated fluid columns at greatly reduced driving frequency compared to typical SBSL, resulting in much larger bubbles and dramatically “brighter” light emission. Gaitan et. al.[40] conducted SBSL events at high ambient pressures and acoustic amplitudes, likewise reporting “brighter” events.

Single-shot methods differ from SBSL variants in that a bubble is nucleated or inserted into an acoustic field by some external means. As a result, its contents and dynamics are not governed by the diffusional, chemical, and inertial equilibria which act

over long time periods and many oscillation cycles, so most of the parameter limitations of SBSL can be avoided. The dynamics of interest occur during the first one or two collapse cycles, and the subsequent breakup or dissolution of the bubble is of no consequence. Lauterborn et. al.[12,41,42] use low energy laser breakdown to nucleate a bubble in a resonant acoustic field which has an amplitude greater than would normally allow a stable bubble, and report increased "luminescence yield". Kappus et. al.[43] inject a large bubble with a needle and drive it to collapse with a 2.5 bar plane wave, reporting an asymmetric collapse and a long (150 ns), high power (100 W) luminescence emission with a temperature of about 10^4 K. Several groups[44–48] have used high energy laser breakdown in liquids at a static pressure of 1 bar or more to initiate a cavitation event, generally with poor symmetry governed by the shape of the laser breakdown plasma, which provides all the energy for the event. These events produce weak luminescence at relatively low temperature.

Each of these methods clearly produces modified dynamics and larger or longer stagnation events, but no study reports a measured stagnation energy density higher than found in typical SBSL. Many of these studies characterize the increase in collapse intensity by reporting an increase in the power, energy or photon count of the emitted light. However, it is not clear whether changes in light output are due to changes in the temperature, size, or duration of the stagnation plasma. To illustrate this, consider a spherical plasma of fixed mass, temperature T, and radius R. Blackbody radiant power scales with T^4R^2, while energy density scales with TR^{-3}. Clearly, light output is uncorrelated to energy density.

In addition, while each of these methods avoids some of the limitations of SBSL, some limitations remain and new limitations are introduced. In all the methods of the first class, SBSL variants, the process begins with a stable SBSL bubble. This means that the gaseous contents of the bubble are determined by the same diffusional and chemical

equilibria as SBSL. The acoustic drive conditions are perturbed to provide more energy to the event, but the quantity and species of the gas inside the bubble cannot be directly controlled. The single-shot methods do not necessarily have this limitation, but all those described above introduce a new limitation – asymmetry. As many of the cited studies show, any bubble that receives a significant amount of its energy from laser breakdown, or is driven by a plane wave instead of a spherically symmetric one, will have significant asymmetry during collapse. This leads to a large, disorganized stagnation event of long duration. Such an event may emit a comparable or even greater amount of light than a symmetric collapse of similar energy, but the energy density is significantly lower.

CHAPTER II

ENERGETIC CAVITATION COLLAPSE

Motivation

The energy focusing that occurs during controlled cavitation collapse is of interest both to basic science and to the industrial and scientific applications described in the first section. If the stagnation energy density could be scaled to greater values than observed to date, which seems plausible if the appropriate initial conditions can be generated, the phenomenon could find new applications in the study of high energy density plasmas[49] (generally defined as those which exceed 1 Mbar of pressure). These conditions are relevant to planetary and astrophysics, and to the dynamics of inertial confinement fusion implosions. It is even conceivable[50] that the event could be employed to generate fusion reactions, resulting in a nanosecond pulsed neutron point source valuable for imaging.

High energy density plasmas can generally be produced only in massive facilities[51–53] which require megajoules of energy and have repetition rates on the order of one per hour or day. The ability to probe these conditions at high rep-rate in a tabletop device could lead to acceleration of progress in the field. The object of the present work is to probe the limits of energy focusing that might be achieved with cavitation collapse, and to demonstrate the production of a high energy density plasma in a tabletop device.

Theory

We outline here a simple theory[1,2,5,54] of energetic cavitation collapse (ECC) designed to be implemented in a physical device and maximize energy focusing at arbitrary scale. As described above, we assume a spherical bubble of radius $R = R_0$ is

initially stationary in an infinite liquid with uniform density ρ_0 and temperature T_0. The bubble contains saturated vapor at equilibrium with the liquid at pressure $p_{V0} = f(T_0)$ and a small quantity of non-condensable gas at partial pressure $p_{G0} \ll p_{V0}$. This bubble is then driven to collapse by a step increase in far-field liquid pressure to some large value $p_\infty^* \gg p_{V0}$. The collapse energy and time are given by equations (6) and (7). A stagnation event brings the collapse to a halt when the interior pressure becomes comparable to the inertial forces by isentropic and shock compression.

To compare experimental measurements with theory, we shall require a simplified but accurate model for the bubble radius evolution during the collapse. As we shall discuss further below, strong collapses accelerate to velocities above the sound speed in the liquid, and liquid compressibility effects become important. This invalidates equation (1). The entire bubble radius evolution of even very energetic collapses can be modeled quite accurately by the theory of Gilmore[55] which includes liquid compressibility to second order. However, for the experimental purposes here, it simpler to divide the collapse into distinct regimes: acceleration, incompressible coasting, transition, compressible coasting, stagnation, and shock emission.

Acceleration occurs while the bubble radius proceeds from R_0 to $R_0/3$ (losing 96% of its volume). During this phase, the applied pressure does work on the bubble and the energy of the fluid flow increases. This is followed by the incompressible coasting phase, where the total kinetic energy is roughly constant and the liquid can be assumed incompressible. Total kinetic energy[2] is given by

$$E = 2\pi\rho_0 U^2 R^3 \tag{11}$$

where $U = \dot{R}$ is the bubble wall velocity, and the bubble radius as a function of time is given by

$$R_i = \left(\frac{E}{\rho_0}\right)^{1/5} (t_i - t)^{2/5} \tag{12}$$

(subscript i denotes incompressible). Then there is a transition phase where the liquid compressibility becomes increasingly significant.

Once the fully developed compressible flow is established[10] the bubble radius is given by

$$R_c = A_c(t_c - t)^{n_c} \tag{13}$$

(subscript c denotes compressible). For water, Hunter[10] finds that $n_c = 0.555$ and A_c is a constant which depends on collapse energy. The stagnation event then occurs at a radius which depends on gas content and symmetry. Finally, a shock wave is emitted, shown by Hunter to have radius

$$R_s = A_s(t - t_s)^{n_s} \tag{14}$$

where A_s and n_s are constants while the shock is strong (subscript s denotes shock). Each of these three forms includes a time offset (t_i, t_c, and t_s) which corresponds to a hypothetical instant of zero radius. These times are unphysical and only indirectly related to one another.

The sequence of events designed to approximate ECC and demonstrated here is: 1. In degassed water held at its vapor pressure, a bubble is nucleated by laser breakdown. 2. The bubble coasts to its maximum radius of ~2 mm in ~1 ms and contains primarily vapor. During this slow, decelerating growth, spherical symmetry is stabilized by inertial, viscous, and surface tension effects[1]. 3. Piezoelectric drivers supply a symmetric pressure step function, driving the bubble to collapse. 4. The collapse stagnates, emitting light for a few nanoseconds. 5. A strong shock carries away most of the collapse energy. 6. The bubble disintegrates into a cloud of micro-bubbles on

rebound as a result of the Rayleigh-Taylor instability[1]. 7. Continuously circulating fluid carries away the contaminating bubbles and the process can be repeated.

Apparatus

A flattened, top, cross-section schematic view of the device designed to conduct ECC events[54] and arranged for spatial streak imaging is shown in Figure 1. The central vessel (black) is heavy stainless steel, has an inner radius of about 25 mm and is fitted with four 25 mm diameter fused silica optical windows. Degassed, deionized, room temperature water fills the vessel. A photo is shown in Figure 2.

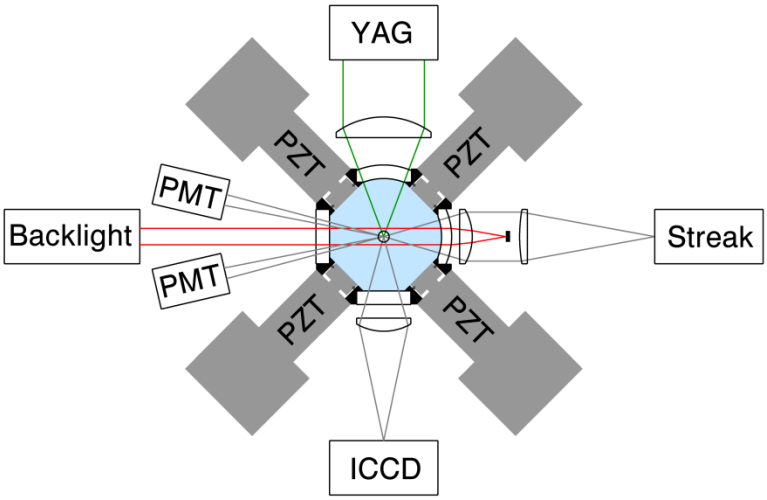

Figure 1. ECC apparatus schematic.

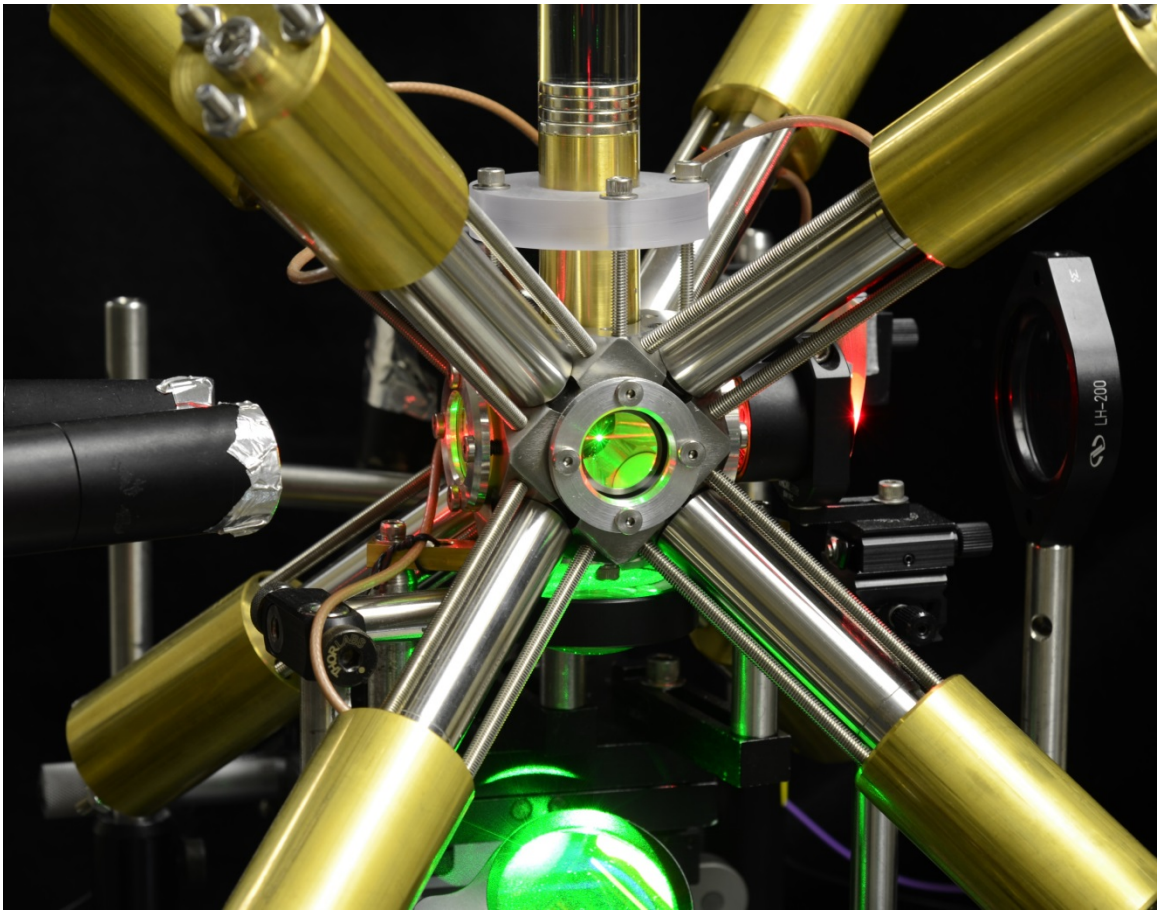

Figure 2. ECC apparatus photo. The green point of light at the vessel center is the nucleation laser breakdown. The horizontal red line that intersects it is the 100 mW backlight laser used to illuminate the bubble for high speed imaging. This image was taken before the device was reconfigured to install the circulation system.

A closed circulation system shown in Figure 3 continuously draws from the bottom of a quiescent fluid column with its free surface held at the vapor pressure by a vacuum pump. A circulation pump is situated about one meter below the vessel and raises the liquid pressure to 1 bar, causing any micro bubbles to shrink or dissolve. The liquid enters the bottom of the vessel through an 18 mm diameter sintered metal filter with 2 μm porosity which eliminates turbulence, filters out remaining micro bubbles, and provides a pressure drop back to vapor pressure. The liquid exits the vessel at the top, and is returned to the top of the quiescent fluid column. The elevation of the return outlet

is varied to precisely control the pressure in the vessel, which is maintained just above the level which causes spontaneous cavitation, i.e. at or slightly below the vapor pressure (~2.3 kPa).

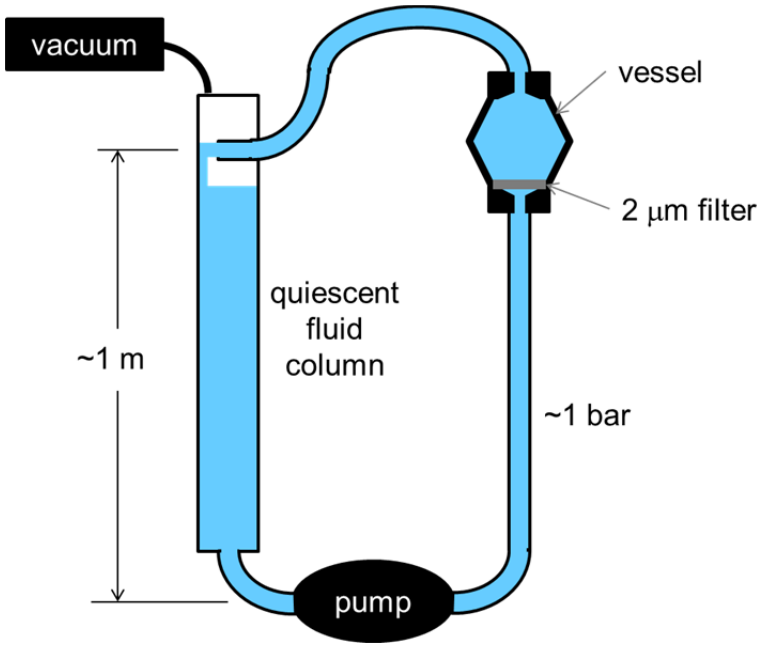

Figure 3. Circulation system schematic.

The output of a Continuum Surelite III doubled YAG was passed through a variable attenuator consisting of a rotatable half wave plate and thin film polarizer, then clipped with a 1 mm diameter aperture to further reduce the pulse energy and select a high quality portion of the beam. The remaining 1 mm diameter beam was spatially filtered and expanded 20X to about 20 mm in diameter, then focused with an aspheric objective lens through a custom spherical dome vacuum window, resulting in a focusing angle of about 30 degrees and a presumed diffraction limited spot of about 3 μm at the vessel center. The bubble was nucleated with a 9 ns, ~1 mJ pulse at 532 nm, just above the breakdown threshold in water[56]. It was found that these parameters produced the

most spherical bubble. Smaller focusing angles, short pulses, or larger pulse energies all create an oblong plasma and asymmetric bubble. It is also desirable to minimize the laser pulse energy to minimize the creation of non-condensable plasma recombination products. Pulse energy was varied in the range of 1-5 mJ to produce an expanding bubble with 2-5 μJ of kinetic energy which grows to a maximum radius of 1-2 mm radius in 0.5-1 ms. Asymmetry was less than 1% during the growth phase as measured by 100 kHz imaging with a CMOS camera.

The pressure pulse was provided by a symmetric array of 8 piezo-electric elements (PZT) custom designed for pulsed operation (Piezomechanik PIA1000/10/60 VS20 VAg). Each active PZT element is 10 mm in diameter by 60 mm in length, and enclosed in a stainless steel sleeve. The PZT material is a ceramic, and does not have significant tensile strength. Under pulsed operation, large tensile stresses will occur during the resonant ringing after the pulse. To protect against this, the enclosure is designed to apply a compressive preload to the PZT element with a stack of Bellville washers. The PZT elements were coupled to the water via 16 mm diameter o-ring sealed aluminum pistons. A brass seismic mass was placed behind each PZT element to provide a reaction force so that acoustic pulse energy was not lost.

The dimensions of the PZT elements were determined by an optimization study which considered the acoustic pulse amplitude, duration, and rise time, and the resulting power consumption and bubble collapse time. A schematic of the piezo-acoustic driver coupling is shown in Figure 4a. The aluminum piston is impedance matched to the PZT and acoustically passive, so it is neglected here. Throughout the following discussion, the subscripts M, P, and W refer to the seismic mass, PZT element, and water, respectively. L refers to the axial length of each element, D to the diameter, and $A = \pi D^2/4$ to the cross-sectional area. I_{AM}, I_{MP}, and I_{PW} refer to the interfaces at the air/seismic mass, seismic mass/PZT, and PZT/water boundaries respectively.

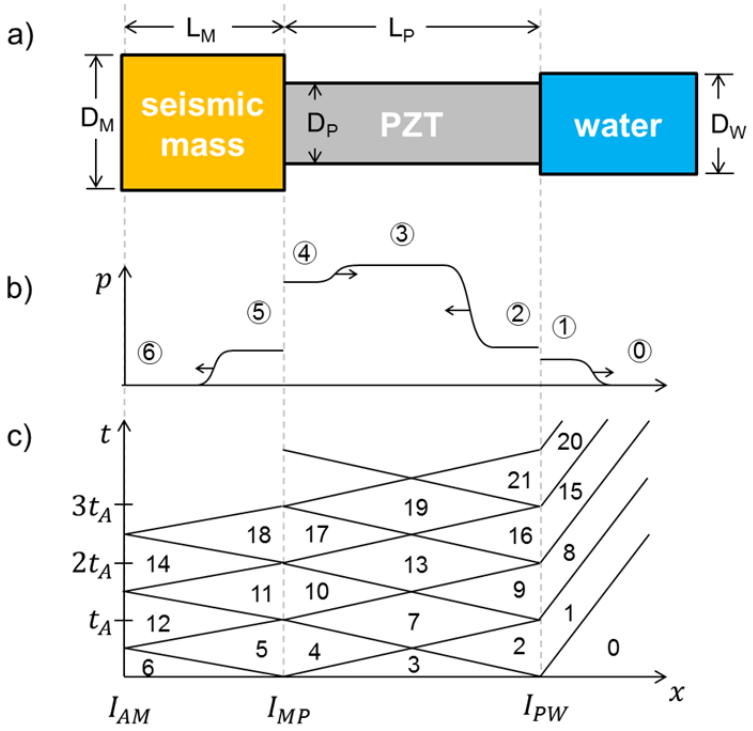

Figure 4. Schematic of the piezo-acoustic driver coupling.

Electrically, the PZT element acts as a capacitor which stores charge $Q = CV$ where C is the capacitance and V is the applied voltage. Mechanically, the effective length of the PZT element changes by a fraction proportional to Q. These PZT elements are designed to operate in a pulsed mode, where they are charged quickly compared to the acoustic time, the time required for a longitudinal wave to travel the axial length of the element, given by $t_A = L_P/c_P$ where c is the sound speed. In this mode, the material is effectively "pressurized" to a stress proportional to Q, then relaxes acoustically.

Figure 4b shows the initial wave propagation shortly after the PZT is charged to pressure $p_3 \propto Q$. Compression waves propagate into the water and seismic mass, and rarefaction waves propagate into the PZT. The seismic mass is designed to have a

length which satisfies $t_A = 2L_M/c_M$ so that the wave which originates at I_{MP} and reflects from I_{AM} does not arrive at I_{PW} until $2t_A$.

An xt diagram for the first four acoustic times is shown in Figure 4c, with numbered regions of uniform pressure (the first six correspond to Figure 4b) separated by boundaries and wave trajectories. A system of equations can be written by applying continuity and force balance at each interface. For example, $u_2 = u_1$ and $p_2 A_P = p_1 A_W$, where u is particle velocity and p is pressure. The isentropic wave relation[57] $\Delta u = \Delta p/z$ also applies across each wave, where $z = \rho c$ is the acoustic impedance of the material. Solving this system with appropriate initial conditions ($u_0 = u_3 = u_6 = 0$ and $p_0 = p_6 = 0$) we find

$$p_3 = p_1 \left(\frac{z_P}{z_W} + \frac{A_W}{A_P} \right) \tag{15}$$

$$p_8 = p_1 \left(A_M z_M - A_P z_p \right) / (A_M z_M + A_P z_P) \tag{16}$$

From equation (16) we see that if the area and impedance of the seismic mass are large compared to the piezo element, then $p_8 \approx p_1$ and this pressure is maintained at the water interface until $2t_A$. After that time the pressure at the water interface will become negative, and the solution becomes invalid since the water is likely to cavitate and violate the continuity assumption.

To satisfy the conditions discussed above, the seismic mass was constructed of 37 mm diameter brass, a material chosen for its large impedance and relatively low sound speed among metals (this allows it to be relatively short).

Per manufacturer specifications, the PZT material has a density of 7.8 g/cm^3, sound speed of 2600 m/s, and at 1000 V (the maximum allowable potential) develops a stress of about 300 bar. Water at STP has a density of 1 g/cm^3 and sound speed of 1450 m/s. Given the piezo and water (piston) diameters stated above, the bracketed quantity in equation (15) evaluates to 16.5, and the amplitude of the acoustic pulse in the water is

about 18 bar. At this drive pressure, a bubble of the maximum achievable radius (about 2 mm) will collapse in 43 μs as given by equation (7). Thus the length of the PZT elements was set at 60 mm, so that $2t_A = 46$ μs and the pressure remains positive throughout the duration of the collapse. The 8 piezo elements at these dimensions have a combined capacitance of about 1.4 μF. A 200 A current pulser was selected to charge them to 1000 V in about 9 μs, a fraction of the collapse time.

With the physical system assembled, the pressure response at the center of the water filled vessel was measured with an uncalibrated fast transducer (Kistler 601A) in the absence of a bubble. The rise time was found to be 3 μs, shorter than expected, and the duration of the positive pulse 95 μs, longer than expected, probably due to confinement and reverberation of the pulse within the steel vessel. The amplitude of the pulse was found to be linearly proportional to the charging voltage as expected. At 1000 V it had a magnitude of about 22 bar, inferred from observed bubble collapse times and equation (7). This pressure is also slightly higher than expected.

Diagnostics

The primary diagnostic was stroboscopic and streak imaging with collimated laser backlight and a dark-field objective configuration. The illustrative diagram in Figure 5 (not to scale) shows representative rays of the collimated backlight deflected by the bubble and density gradients[10] of the compressible collapse phase. The labeled rays in this figure will be discussed further below. The infinity corrected plan-apochromatic objective has a focal length of $f_0 = 40$ mm, a numerical aperture of 0.23, and resolves about 2 μm. Imaging lenses of various focal lengths f_i in the range of 300-1000 mm were used to achieve various magnification *M* in the range of 7.5-25. The spherical-dome vacuum window shown in Figure 1 is designed to be optically passive and is not shown in Figure 5.

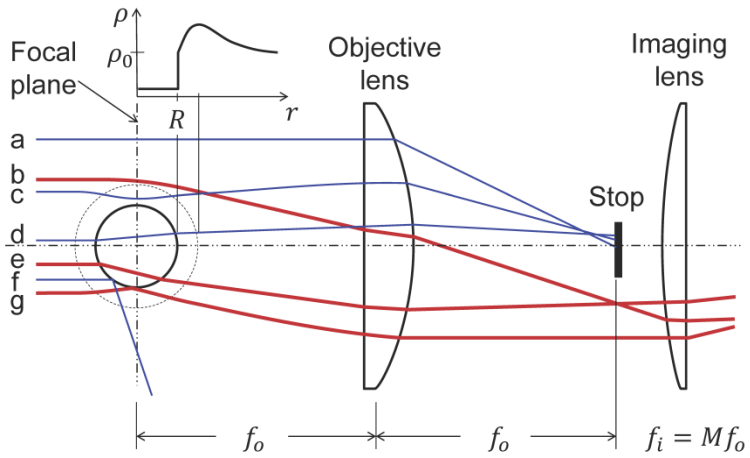

Figure 5. Diagram of imaging optics.

Figure 1 shows the diagnostic arrangement for streak imaging. In this case, the backlight was provided by continuous illumination with a 660 nm, 100 mW diode laser (Coherent OBIS). The primary dark-field image was focused onto the slit of a streak camera (Hamamatsu C7700). A second intensified camera (ICCD) was used to continuously monitor the stagnation location and ensure that it remained centered in the focal plane of the streak camera slit.

For stroboscopic imaging the backlight was pulsed and the streak camera was replaced with an ICCD camera which was gated to collect several exposures on a single image. For slow dynamics the backlight was provided by the Coherent OBIS modulated with a Stanford Research DG645 delay generator, an arrangement capable of producing 2 ns pulses at up to 10 MHz. To capture fast dynamics, the backlight was provided by a Coherent Chameleon Ultra II Ti:Saphire oscillator producing about 600 W at 700 nm in 140 fs pulses at 80 MHz.

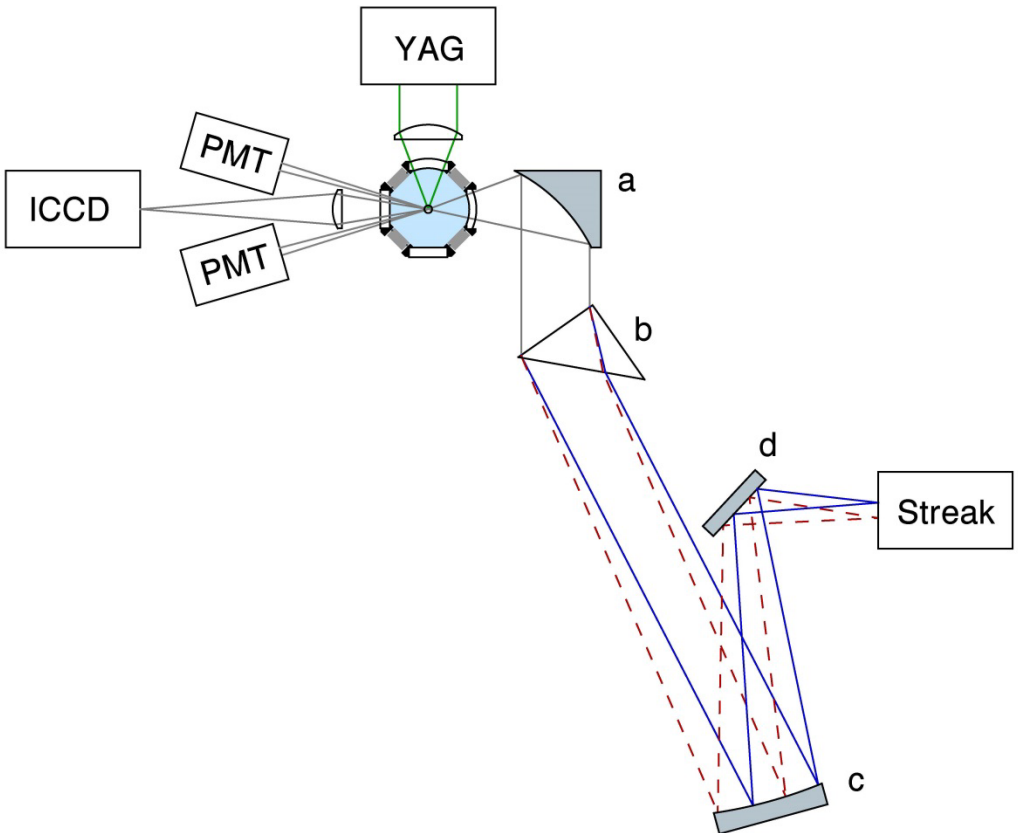

Figure 6. Schematic of diagnostics arranged for spectral streak imaging with a custom refractive spectrometer, shown roughly to scale with representative rays at 280 nm (solid blue lines) and 700 nm (dashed red lines).

A time resolved spectral diagnostic was assembled by coupling the streak camera to a custom refractive spectrometer as shown in Figure 6 and recording the self-emission luminescence of the stagnation plasma. The light is collected with a 50 mm diameter aluminum off-axis parabolic mirror (a) with a focal length of 50.8 mm and off-axis angle of 90°, giving an effective focal length of 101.6 mm and a collection aperture of about f/2. The collimated light is dispersed with a 60 mm, 90° fused silica prism (b), then focused with a second aluminum off-axis parabolic mirror (c), 60 mm square with focal length 275 mm and effective focal length 279 mm. Finally, it is directed toward the streak camera slit by a planar aluminum mirror (d). This configuration fit the spectrum 280-700 nm on the 12 mm streak slit. Refraction was chosen over diffraction to

maximize efficiency and avoid the overlap of diffractive orders. This spectrometer was calibrated with the known dispersion relation of fused silica, a HgAr atomic line lamp (Oriel), and a calibrated deuterium/halogen broadband source (Avantes). The dispersion calibration was accurate to about 1 nm. The spectral sensitivity calibration is specified at ±10% overall, but local errors of up to 26% are suspected below 430 nm, as discussed below in the Figure 14 caption.

A second, simpler time resolved spectral diagnostic was employed for verification as well as for continuous spectral monitoring during experiments in which the spectrometer was not installed. This diagnostic consisted of two photomultiplier tubes (PMT, Hamamatsu R9880U) with 100 nm bandpass filters centered at 330 and 780 nm. This allowed continuous monitoring of luminescence intensity and temperature with 1 ns time resolution. This signal also gave an accurate indication of the stagnation time. This was compared to the known arrival time of the drive pressure pulse to calculate the total collapse time t_{TC} for each event.

A second 1 mW CW backlight laser (not shown in Figure 1) partially blocked by the bubble and focused onto a photodiode provided a radius vs. time signal used to anticipate the stagnation event and provide a trigger signal for the other diagnostics. It was possible to predict the stagnation moment with accuracy of about 20 ns.

CHAPTER III

EXPERIMENTAL RESULTS

Parameter study

We will begin the discussion of experimental results with a parameter study which explores the limits of the apparatus and spans two orders of magnitude in collapse energy. This study employs simple, low resolution diagnostics. In the subsequent section, we will present a more detailed analysis of a typical event with fixed parameters corresponding to the largest, most energetic event which can be reliably produced. Such an event yields the highest resolution diagnostic data.

With the apparatus described here, the primary parameters available for variation include the energy of the nucleation laser pulse, time delay between nucleation and application of the pressure pulse (i.e. bubble growth time), and the voltage applied to the piezos. Together, these effectively control the initial bubble radius R_0 and the drive pressure p_∞^*. These in turn determine the single physically relevant parameter, collapse energy E, given by equation (6). Practical considerations including gravitational effects and the real temporal profile of the acoustic pulse necessitated that the bubble growth time be held between 500 and 1000 μs and the collapse time between 35 and 45 μs for consistent results. For example, at longer growth times, buoyancy induced asymmetry would perturb the growth, at shorter collapse times the rise time of the acoustic pulse would become significant, and at longer collapse times the duration of the acoustic pulse is insufficient. Thus the variable parameters were chosen to keep within these boundaries while producing a broad range of collapse energies.

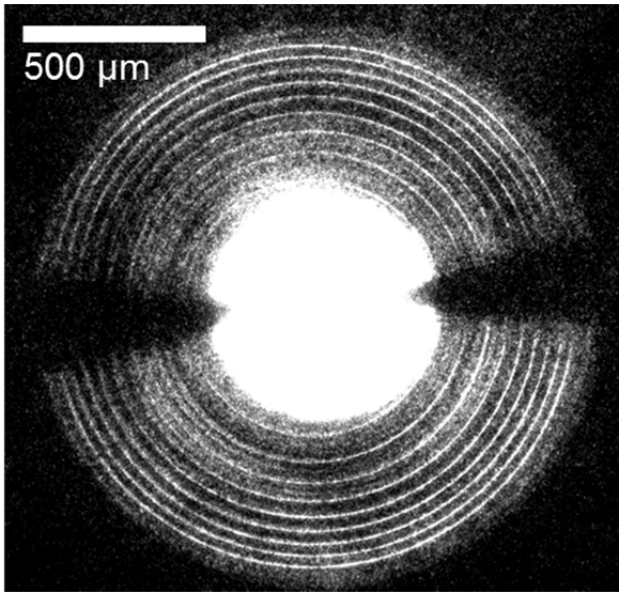

Figure 7. Stroboscopic imaging of the incompressible coasting collapse phase backlit with 2 ns pulses at 1.25 kHz (800 ns interframe time). The saturated region in the center is due to laser backlight which is weakly refracted through the center of the bubble. It is off center due to a slight angular misalignment of the laser relative to the imaging optics – this does not represent asymmetry of the bubble itself.

Figure 7 shows a typical “slow” stroboscopic image taken during the incompressible coasting collapse phase. To quantify collapse energy from such an image, the radius vs. time data can be fit to equation (12). Such fits are shown in Figure 8a for about 30 calibration events. Fits are also shown for collapse energy (b) along with drive pressure (c) and initial radius (d) calculated from equations (6) and (7) with the measured collapse energy and time. The root-mean-squared error (rmse) is given for each fit. In all subsequent experiments, the collapse energy was determined from the fit shown in Figure 8b, given the applied voltage and measured collapse time.

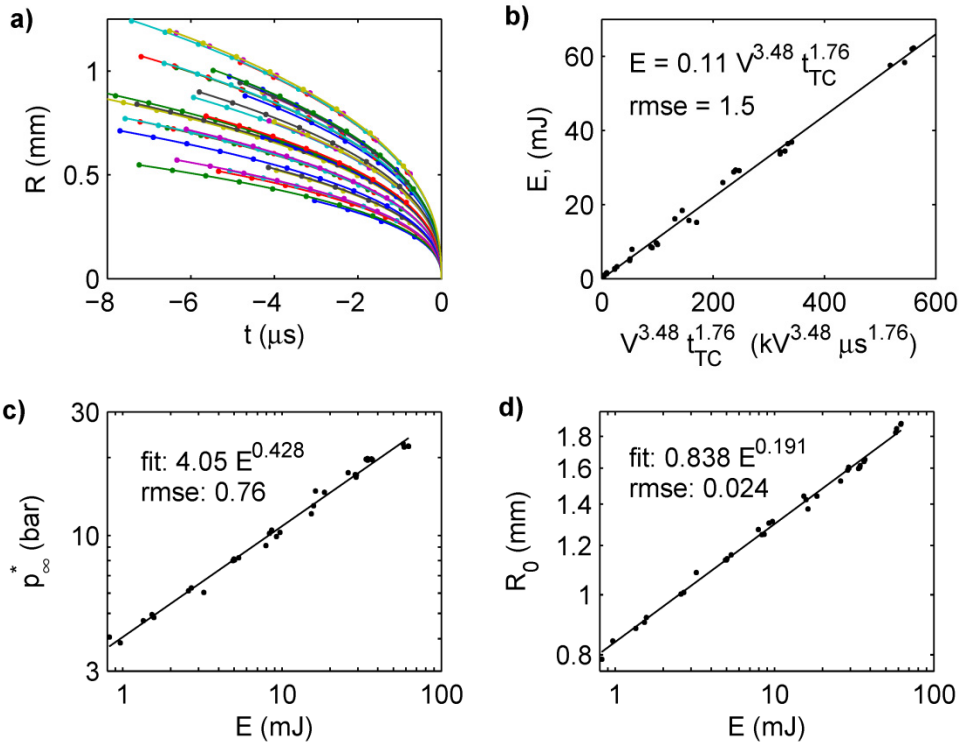

Figure 8. Radius vs. time fits (a) to data taken from slow stroboscopic images (dots) for about 30 calibration events. Fits give analytical relations for collapse energy (b), drive pressure (c), and initial radius (d). Note that the units for voltage and collapse time used in the fits are kV and μs respectively.

Once the collapse energy had been calibrated, about 100 events were recorded at various energies with two luminescence diagnostics. The first was direct imaging with an ICCD camera, from which the full-width half-max (FWHM) radius of the emitting region could be measured. One of two different filters was used on this camera, either an RG 590 long-pass filter to image red light with wavelength longer than 590 nm, or a UG 11 band pass to image UV light in the range 250-380 nm. The dominating uncertainty in this measurement is the unknown magnification of the images by refraction in the time-varying density gradients in the liquid surrounding the bubble. As discussed in Section IV, this uncertainty may be on the order of 20%.

The second diagnostic was the pair of PMTs with 100 nm bandpass filters centered at 330 and 780 nm, respectively. Figure 9 shows typical data collected with these PMTs. By measuring instantaneous spectral power at two wavelengths, and assuming that the source is a spherical blackbody, it is possible to calculate both the temperature and radius of that source[22].

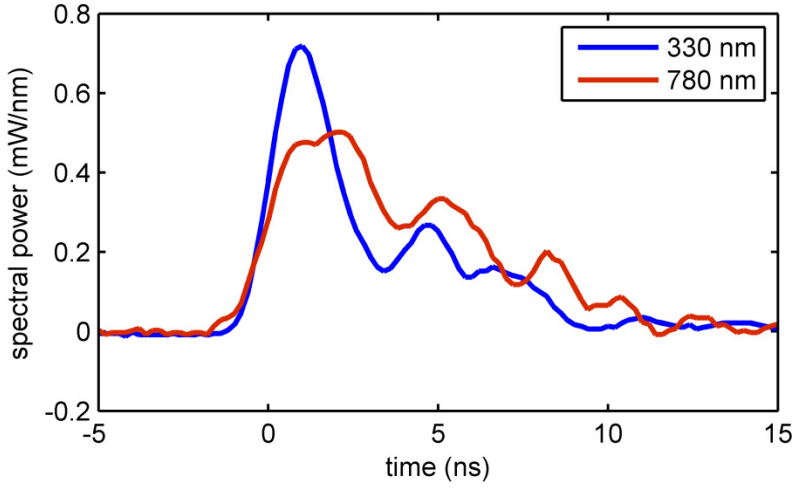

Figure 9. Typical luminescence emission as measured with two PMTs with 100 nm bandpass filters centered at 330 and 780 nm. The time resolution is about 1 ns. The oscillation observed after the peak is likely due to electrical ringing, and is not physical.

For an estimate of the temperature uncertainty of this type of measurement, consider the sensitivity of blackbody temperature to the ratio of spectral intensity at these two discrete wavelengths. This ratio can be expressed by

$$R_B = \frac{B_{\lambda 1}(T)}{B_{\lambda 2}(T)} = \left(\frac{\lambda_2}{\lambda_1}\right)^5 \frac{\left(e^{\frac{hc}{\lambda_2 k_B T}} - 1\right)}{\left(e^{\frac{hc}{\lambda_1 k_B T}} - 1\right)} \tag{17}$$

where B is spectral intensity, R_B is the ratio of spectral intensity at the two wavelengths, λ is wavelength, h is the Plank constant, c is the speed of light, k_B is the Boltzmann

constant, and T is temperature. Solving numerically, one finds that in the temperature range of 6000-14000 K, the partial derivative $\partial T/\partial R_B \approx 1000$ K. Assuming that the spectral intensity calibration of the detectors is accurate to $\pm 10\%$, the temperature uncertainty is about ± 220 K. At lower temperatures this uncertainty increases rapidly. At 5000 K it is about ± 400 K and at 4000 K it is about ± 810 K.

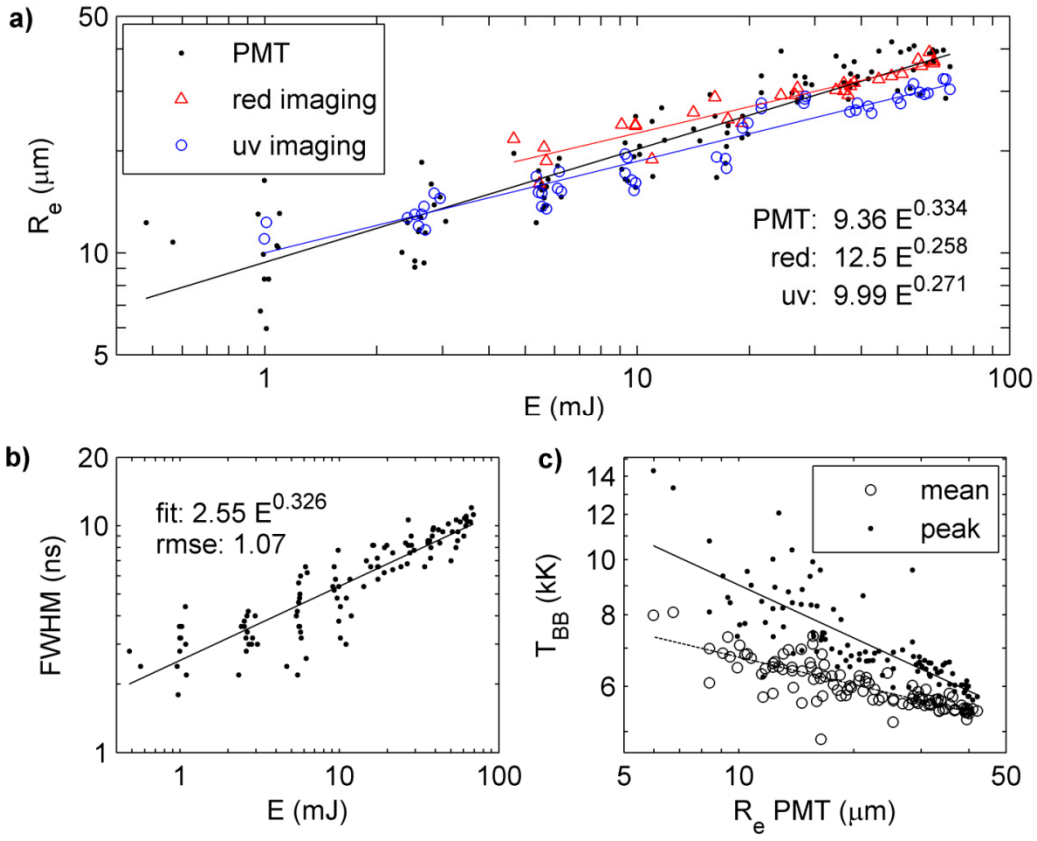

Figure 10. Luminescence data over two orders of magnitude in collapse energy, including FWHM emitting radius R_e (a) measured by the ICCD camera with two different filters and by the PMT method, the FWHM luminescence duration (b), and the peak and time-averaged blackbody temperatures T_{BB} (c).

Figure 10a shows the measured luminescence radius over two orders of magnitude in collapse energy. Measurements by the two methods (ICCD camera at

different wavelengths and the dual PMT blackbody method) are consistent. The clear trend shows that at higher collapse energy the luminescence radius (and implicitly the stagnation radius) is greater. This likely indicates that more vapor is trapped in higher energy collapses. This is consistent with the hypothesis that vapor condensation ceases as a result of thermal or diffusive mechanisms[58] when the bubble wall velocity reaches a given threshold. For higher energy collapses, this limiting velocity is reached at larger radius, trapping more vapor.

Figure 10b shows the measured luminescence duration as a function of collapse energy, indicating that higher energy collapses have longer luminescence duration. It is interesting to note that the PMT fit of Figure 10a divided by the fit of Figure 10b gives a constant with a magnitude of about 3.7 μm/ns (equivalent to km/s). This suggests that the plasma cools by an acoustic process, and that the sound speed (directly related to the thermodynamic state) in the stagnation plasma is roughly independent of collapse energy. This conclusion is bolstered by the temperature data shown in Figure 10c. This data shows only a weak trend with collapse energy. It is plotted against emission radius instead, with which it shows a clearer, though still mild, trend. Combined with qualitative observation of the plasma images, this suggests that the strongest indicator of plasma temperature is collapse symmetry. Less symmetric collapses produce a larger but less organized and lower temperature plasma. Collapses with good symmetry produce a stagnation temperature which is nearly independent of collapse energy. Unfortunately, “good symmetry” is difficult to define, especially since only 2D images are available of the 3D event. Here it is loosely defined as those collapses in which the stagnation plasma appears symmetric within about 10% in a time-integrated 2D image.

From the above discussion we extract two hypotheses. (i) Vapor condensation ceases at a given bubble wall velocity threshold, trapping the remaining vapor. Before this occurs, the bubble interior is composed simply of saturated vapor at equilibrium with

the liquid, and its pressure is a function of liquid temperature only [equation (3)]. (ii) The thermodynamic state of the stagnation plasma is roughly independent of collapse energy.

These two hypotheses can be shown to be consistent by the following scaling argument. Rearranging equation (11) and substituting the threshold velocity U_{cs} (the fixed velocity at which condensation stops)

$$R^3 = \frac{E}{2\pi\rho_0 U_{cs}^2} \tag{18}$$

we find that, during the incompressible coasting collapse phase, the bubble wall reaches U_{cs} at a radius R_{cs} which is proportional to $E^{1/3}$. If this saturated vapor is then compressed to a fixed stagnation density which is independent of E, then the stagnation radius must also be proportional to $E^{1/3}$. Indeed, this is precisely the scaling shown by the data of Figure 10a, which spans two orders of magnitude in collapse energy.

This gives strong evidence that, for the pure vapor bubbles studied here, all collapses are essentially self-similar, with the only independent parameter being collapse energy E. This parameter determines the radius R_{cs} at which condensation stops, and thus determines the mass of trapped vapor $m_V = \rho_v \frac{4\pi}{3} R_{cs}^3$ where ρ_v is the saturated vapor density. From that point on we see by again re-arranging equation (11) and substituting the critical velocity and mass of trapped vapor that

$$\frac{E}{m_V} = \frac{3}{2}\frac{\rho_0}{\rho_v} U_{cs}^2 \tag{19}$$

so that the ratio of energy to trapped mass is essentially fixed. Thus the stagnation state can be expected to be the same for a collapse of any energy.

This conclusion is in contrast to SBSL events, in which the fixed quantity and species of non-condensable gas in the bubble interior yield additional independent parameters.

It will now be of interest to estimate the value of the critical velocity U_{cs}. Unfortunately, this cannot be done with the experimental results alone, which reveal the stagnation radius, but not its density (and mass). In the simulation chapter below we will estimate the stagnation density and find that the critical velocity is about $U_{cs} \approx 59$ m/s, much lower than might have been expected[5,58], i.e. roughly the sound speed in the vapor, ~400 m/s.

Typical high energy event

I now present a more detailed analysis of a typical maximum energy event[54], which is driven with 1000 V and has a measured collapse time of 35 μs. The collapse energy is $E = 57$ mJ, as given by Figure 8. The maximum radius and effective driving pressure for this collapse are then $R_0 = 1.8$ mm and $p_\infty^* = 22$ bar, as calculated from equations (6) and (7). Note that this maximum radius cannot be directly observed with the high magnification optics required to resolve the stagnation dynamics, but is consistent with observations of similar bubble nucleation events at low magnification.

Stroboscopic images of the final stages of such a typical event are shown in Figure 11. These 8 exposure images illustrate typical collapse symmetry, and show that low order shape perturbations grow slowly during collapse. This diagnostic was used to tune the individual PZT charging voltages for optimum collapse symmetry. A qualitative threshold symmetry was observed below which a liquid jet forms, creating an off-center, asymmetric stagnation plasma with longer, cooler light emission. Note that symmetry did vary from shot to shot, and that shots with the best symmetry were selected for analysis in this section.

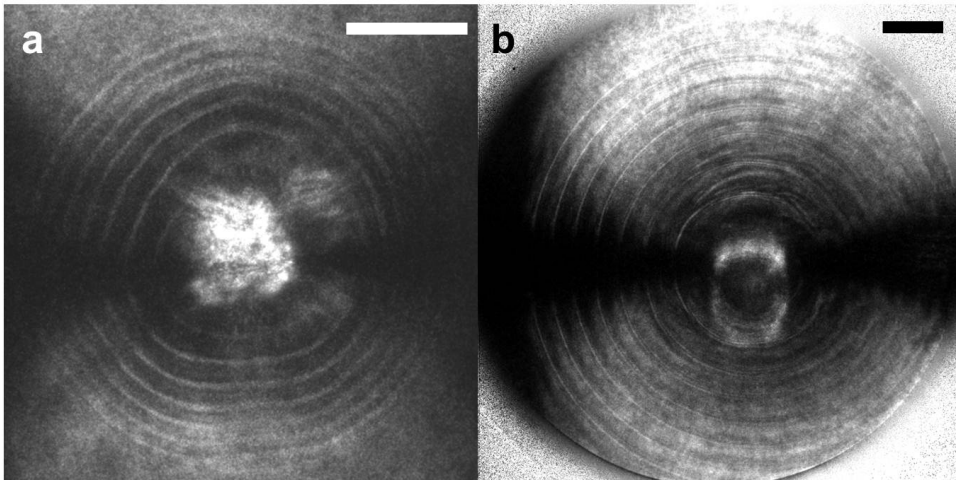

Figure 11. Stroboscopic imaging of a typical event backlit with 140 fs pulses at 80 MHz (12.5 ns inter-frame time). The ICCD camera is gated to collect 8 superimposed exposures. The collapsing bubble (a) is primarily in the transition phase between incompressible and compressible coasting. The reflected shock and slowly rebounding bubble (of a different but similar event) are imaged in (b). Scale bars are 100 μm.

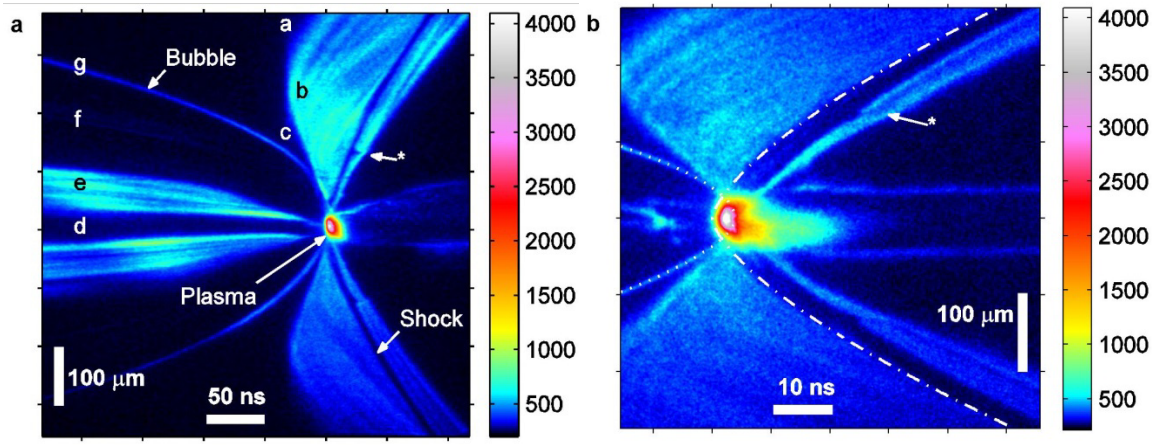

Figure 12. Spatial streak imaging data. A representative single shot spatial streak image which begins during the transition collapse phase (a) has regions labeled which correspond to the rays in Figure 5. Features illuminated by the low intensity laser backlight are rendered in “cold” colors blue and cyan (below 700 counts). The plasma emission can be distinguished by its far greater intensity, rendered in “hot” colors yellow, red, magenta, and white (1000-4096 counts). A similar image entirely in the supersonic collapse phase (b) has time resolution of about 1 ns. The bubble and shock radii are fitted with models R_c and R_s (white dotted and dash-dot lines).

A single shot spatial streak image which begins during the transition collapse phase is shown in Figure 12a, and is labeled to aid interpretation. The bubble wall is accurately imaged by rays similar to g (see also Figure 5) which are moderately deflected by total internal reflection from the bubble wall at glancing incidence. The density discontinuity at the reflected shock is opposite, with higher density behind the shock, so total internal reflection of incident rays does not occur. As a result, the shock appears in the image as a shadow where glancing rays are strongly refracted (not depicted in Figure 5).

We focus our quantitative analysis on Figure 12b, which lies entirely in the compressible collapse regime. The fitted parameter values are A_c=17.2±0.2 μm/ns$^{0.58}$, n_c=0.58±0.03, A_s=19.2±0.2 μm/ns$^{0.68}$, and n_s=0.68±0.03. The fits shown are not quite symmetric. For both the bubble and shock, the top and bottom portion were fit independently (with a common centerline and time offset), and the values reported represent an effective average. The fits were conducted manually, and the uncertainties listed represent the parameter variation which caused an obvious (but subjective) degradation of the fit quality. Other potential sources of uncertainty include imaging system spatial calibration (1%) and streak camera temporal calibration (less than 1%). However, it should be understood that the primary uncertainty is the magnification of the streak images by refraction in the time-varying density gradients in the liquid surrounding the bubble. As discussed in Section IV, this uncertainty may be on the order of 20%.

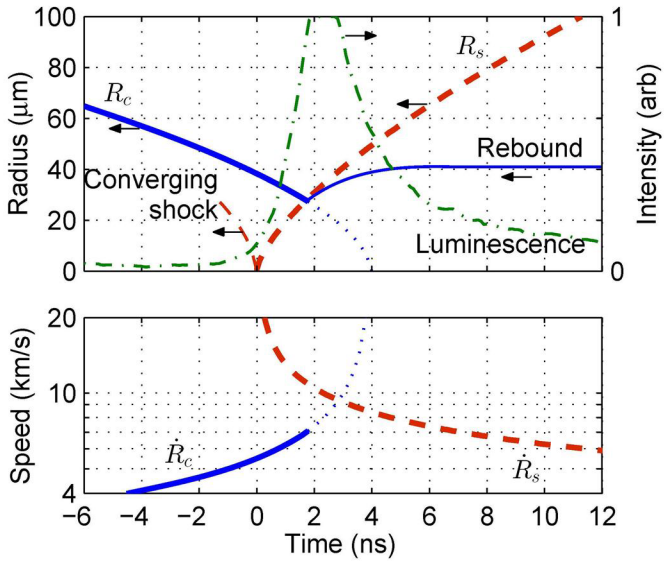

Figure 13. The fits from Figure 12b plotted along with the luminescence intensity at the bubble center (top). The zero of time is set to the hypothetical moment of zero shock radius t_s , which also corresponds with the onset (10% of peak) of plasma emission. The hypothesized converging shock and bubble rebound are sketched for illustration. The bottom plot shows the magnitude of the derivatives of these fits.

Figure 13 shows the bubble and shock fits R_c and R_s along with the plasma emission (luminescence) intensity at the centerline of the image. The bubble and shock intersect at a radius of 28 μm, which brings the collapse to a halt. The remainder of the bubble fit is dotted to indicate that it is unphysical. The apparent rise-time of the plasma emission is roughly 1 ns, equal to the resolution of the measurement, and it begins slightly before the bubble and shock intersect. In Figure 12b it appears that the emission begins at the center of the bubble and propagates outward with time. From these observations I suggest that the plasma emission is initiated by the reflection of a converging compression wave which leads the bubble wall and steepens into a shock as predicted by Wu and Roberts[15]. The presumed approximate form of the converging shock and the rebounding bubble are also sketched in Figure 13. (Neither are visible in the data, though the final ~40 μm quasi-static radius of the bubble is).

Figure 13 also shows the velocity magnitude of the bubble wall and the reflected shock wave, which crosses into the liquid at 1.8 ns. At that instant, the liquid is moving inward at R_c=7 km/s and the shock outward at R_s=11 km/s, so the velocity of the shock relative to the upstream fluid is u_s=18 km/s. The shock is unsupported by any energy source so it has the character of a blast wave[49] (shock compression followed immediately by a rarefaction), and the hot emitting plasma in the bubble interior quenches quickly after the shock enters the liquid. Likewise, as it enters the liquid the shock nearly reverses the inward flow, but the trailing rarefaction almost immediately decelerates it back to near zero in the lab frame. This is predicted by Wu and Roberts[15] and observed here by the nearly stagnant bubble radius after the wave passes. Unfortunately, the fluid velocity immediately behind the shock front is not directly measured. However, we may apply an approximate theory in the strong shock limit[49] since the ratio of pre-shock (~100 kbar) to post-shock (~Mbar) pressure is roughly 10. The post-shock pressure is then $p_s = \rho_0 u_s^2$ or 3.2 Mbar. A conservative lower bound for the shock pressure can be found from exact theory[49] by recognizing that the particle velocity $u_p > 7$ km/s since the liquid is certainly arrested if not reversed. This lower bound is then $\rho_0 u_s u_p = 1.3$ Mbar.

It bears re-emphasis that the primary uncertainty in the velocity measurements is the magnification of the streak images by refraction in the time-varying density gradients in the liquid surrounding the bubble. As discussed in Section IV, this uncertainty may be on the order of 20%, which would lead to uncertainty of up to 69% in the pressure estimates above.

Another interesting feature of the spatial streak data is the disturbance in the shock wave at about 25 ns after stagnation and 130 μm radius observed in both panels of Figure 12 (labeled *). This feature may result from a second shock wave, also

predicted by Wu and Roberts[15], which overtakes the first. However, the simulations presented in the next chapter do not predict such a wave, and instead suggest that this feature may be related to phase change (freezing) of the liquid.

Figure 14 shows time-resolved luminescence emission spectra collected with streak imaging. The rise and fall times of the luminescence are slightly longer than in Figure 12, probably as a result of reduced symmetry. (Symmetry could not be monitored while collecting spectral data.) Still, the temperature peaks very early in the event as the reflected shock forms. Intensity peaks later as the radiating shock propagates outward to larger radius. A peak temperature between 10,000 and 14,000 K is typical of all symmetric collapses at various collapse energies. (Collapses with somewhat reduced symmetry do not exhibit this initial temperature peak, but do still exhibit the “plateau” temperature of around 7000 K. See Figure 10 and discussion.) Both temperature and intensity drop abruptly when the shock crosses the bubble wall into the cool liquid. A slow exponential decay in temperature and intensity follows as the hot bubble contents cool. These observations are consistent with the shock focusing mechanism discussed above.

The uncertainty in the temperature measurements shown in Figure 14 is similar to that discussed in the context of equation (17), or about ± 220 K in the temperature range of 6000-14000 K. It should be noted that the spectrometer was not calibrated for absolute spectral intensity, so this data cannot be used to infer the radius of a blackbody emitter.

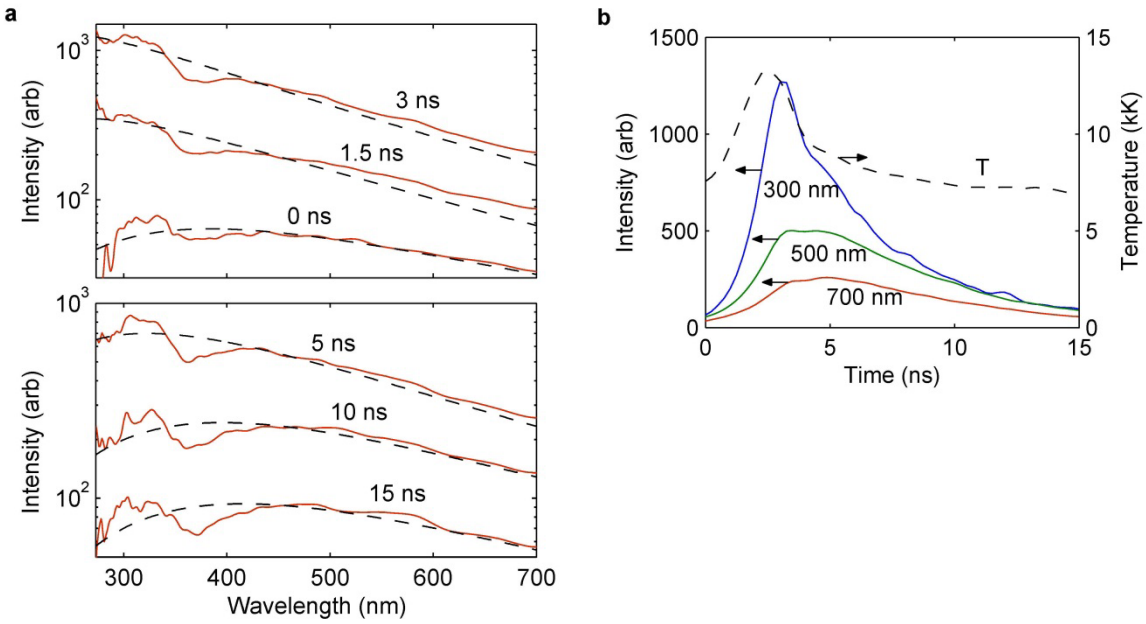

Figure 14. Single-shot, time-resolved spectroscopy of the stagnation luminescence has resolution of about 1 ns. Zero time is defined at 10% peak intensity, so this time scale corresponds roughly to Figure 13 (though it is a separate event.) Instantaneous spectra (solid lines) at several times (a) are shown with blackbody fits (dashed lines). The raw spectral data (not shown) are very smooth; the obvious deviations from the fits at wavelengths below 430 nm result from known imperfections in the calibration provided by the manufacturer of the deuterium/halogen reference lamp. (b) shows fitted blackbody temperature as a function of time, along with intensity at three representative wavelengths.

CHAPTER IV

SIMULATION AND MECHANISMS

Model

Numerical simulations were conducted to gain an understanding of the physical mechanisms at work during ECC and to quantify the thermodynamic conditions generated. Numerous detailed simulations of cavitation collapse exist in the literature[15–17,19,20]. However, these do not apply here for two primary reasons. First, all of these studies have focused on typical SBSL conditions. As discussed above, such collapses have 50 nJ of energy and stagnate at bubble wall pressures below 100 kbar. In contrast, ECC events have a million times more energy (here, 57 mJ), and measurements show that the stagnation pressure may exceed 3 Mbar at the bubble wall. Second, with the exception of Moss[16], all of these studies make assumptions which will be shown here to be entirely invalid. These include the modeling of the liquid with the Rayleigh-Plesset equation and the bubble interior as a van der Waals gas.

Here we model both the liquid and the gas with the full 1D compressible Navier Stokes equations and realistic equations of state. As above, we consider a spherical bubble of radius R centered on the origin of a spherical coordinate system. The equations of motion are:

$$\frac{\partial \rho}{\partial t} + \frac{1}{r^2}\frac{\partial}{\partial r}\left(\rho u r^2\right) = 0 \tag{20}$$

$$\frac{\partial}{\partial t}(\rho u) + \frac{1}{r^2}\frac{\partial}{\partial r}\left(\rho u^2 r^2\right) + \frac{\partial p}{\partial r} = 0 \tag{21}$$

$$\frac{\partial E}{\partial t} + \frac{1}{r^2}\frac{\partial}{\partial r}\left[(E+p)u r^2\right] = 0 \tag{22}$$

where r is the radial coordinate, ρ is density, $E = \frac{1}{2}\rho u^2 + \rho e$ is the total energy density, e is the internal energy, u is the radial component of velocity, and $U = u(R,t)$ is the bubble wall velocity. We employ a moving mesh finite-difference method with 1000 nodes inside the bubble and 2000 outside.

The equation of state of the liquid was modeled with the Tait form[9]

$$\frac{p+B}{B} = \left(\frac{\rho}{\rho_0}\right)^n \tag{23}$$

with values of $B = 3$ kbar, $n = 7$ and $\rho_0 = 0.996\ \mathrm{g/cm^3}$. This equation is accurate to about 100 kbar. The specific heat was assumed constant, $c_p = 4187\ J/kg \cdot K$. The bubble interior was assumed to contain only water vapor, and was modeled with the SESAME tabular equation of state[59] which is maintained by Los Alamos National Laboratory. It includes chemical and electronic contributions and is valid across the entire state space encountered here.

The initial conditions for the simulation were determined from the known values for the typical case: initial radius $R_0 = 1.8$ mm and far-field pressure $p_\infty^* = 22$ bar. The ambient temperature is assumed to be $T_0 = 293$ K. Furthermore, it was assumed that the bubble initially contains only saturated vapor, which condenses freely and remains in thermal equilibrium with the liquid until the bubble reaches some radius R_{cs}. At that instant, condensation stops, the remaining vapor is trapped in the bubble, and the bubble wall is assumed adiabatic.

In practice, it was not necessary to simulate the initial part of the collapse when $R > R_{cs}$. During this early, slow part of the collapse, the liquid can be assumed incompressible and the interior is saturated vapor which simply remains at constant temperature and pressure. Instead, the simulation was begun at $R = R_{cs}$ and the velocity and pressure fields in the liquid were initialized with the analytical incompressible solution[2].

The value of R_{cs}, the radius at which condensation stops, was determined by an iterative process given the measured stagnation radius. Several simulations were run varying R_{cs} until the correct stagnation radius was observed. The stagnation radius measured from the streak image (Figure 13) was $R_{stag} = 28$ μm. However, as will be seen below, we infer that the streak image is magnified by a factor of 1.35 as a result of refraction in the density gradients of the liquid surrounding the bubble during the final stages of collapse. Consequently, the true stagnation radius is $R_{stag} = 21$ μm. With this value it was found that condensation stops at $R_{cs} = 1.2$ mm when the bubble wall velocity is 59 m/s, trapping 30% of the original vapor. This is much earlier than might be expected based on prevailing theories[5,58]. The reason for this is not known.

For comparison and validation, completely separate, simple calculations were conducted for the collapse of an empty cavity with the same initial conditions using both the Rayleigh-Plesset (equation (1)) and Gilmore[55] analytical models. These models have both been widely assumed valid in the context of SBSL[1,5]. However, we show here that the Rayleigh-Plesset equation fails dramatically in the final stages of an energetic collapse, while the Gilmore model, which includes liquid compressibility terms to second order, is much more accurate.

Results

Figure 15 shows bubble wall velocity vs. radius for the final simulation. All three models agree at radii above 300 μm. After that time, the Rayleigh-Plesset (RP) equation, which does not account for liquid compressibility, diverges dramatically from the other two. This is to be expected since the velocities exceed the sound speed in water at STP, $c_0 = 1450$ m/s.

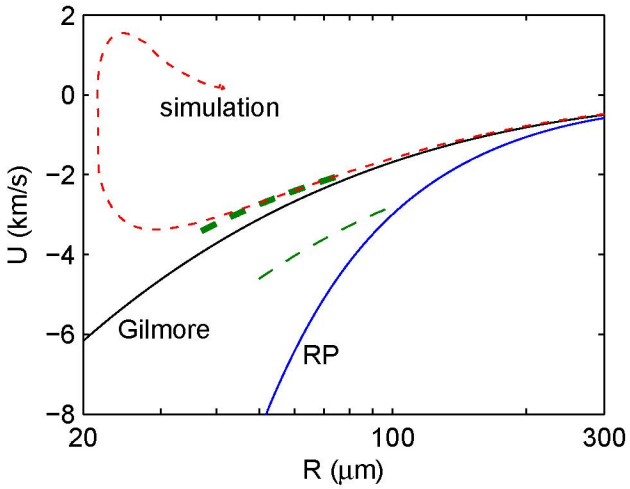

Figure 15. Bubble wall velocity vs. radius as calculated with the Rayleigh-Plesset (RP) and Gilmore models for an empty cavity, and with the full simulation, which includes the vapor inside the bubble. The experimental measurement (green long-dash lines) is shown twice: as measured (thin), and corrected for the inferred magnification (heavy).

Note that a form of the RP equation popular in SBSL work[1,5,60–62]

$$[p_B - p_\infty] = \rho_L \left(R\ddot{R} + \frac{3}{2}\dot{R}^2 \right) + 4\mu \frac{\dot{R}}{R} - \frac{2\sigma}{R} + \frac{R}{c_0}\frac{d}{dt}(p_B) \tag{24}$$

does include a correction for liquid compressibility (the final term). However, that correction only models the acoustic radiation from the bubble wall as a result of pressure changes inside the bubble. This accurately models the energy carried away by the shock wave which is emitted during the stagnation event, but does not account for the conversion of kinetic energy to enthalpy in the liquid due to inertial pressure earlier in the collapse[10]. Even if the bubble contents are modeled and this compressibility correction is included, it begins to affect the solution only after the internal pressure becomes significant (here below about 40 μm). Clearly, the RP equation is an inadequate model for this case, while the Gilmore model compares quite well with the full simulation.

The raw experimental measurement (thin green long dash) shown in Figure 15 clearly does not match any of the models well. As discussed earlier, we suspect that the

experimental images may be magnified as a result of refraction in the density gradients in the surrounding liquid. If we assume this magnification to have a value of 1.35 (constant during this portion of the bubble collapse), we find that the correspondingly corrected experiment (heavy green long dash) matches the full simulation quite well. Up to this point in the collapse we have good confidence in the full simulation, since shock waves have not yet occurred (producing pressures which may exceed the limits of the Tait state equation). As a result, we assume that this magnification is physical. We will investigate this assumption below with optical ray tracing and the calculated density gradients.

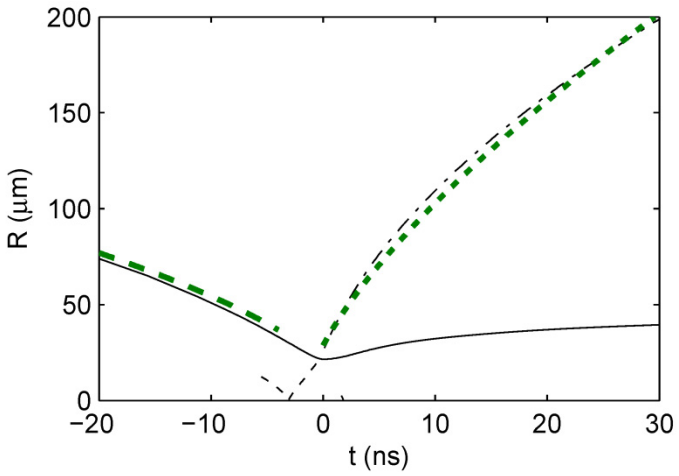

Figure 16. Radius vs. time plot for the full simulation bubble wall (solid line), interior shock (thin dash line), and exterior shock (thin dash-dot line) compared to the experimental measurement bubble wall (heavy green long dash line) and shock (heavy green short dash line).

Figure 16 shows a radius vs. time plot of the full simulation compared to the corrected experiment, giving very good agreement. Note that the experimental magnification has been applied only to the bubble, not the shock, since it quickly moves

outside the region of peak density gradients (as seen below) and is not significantly magnified.

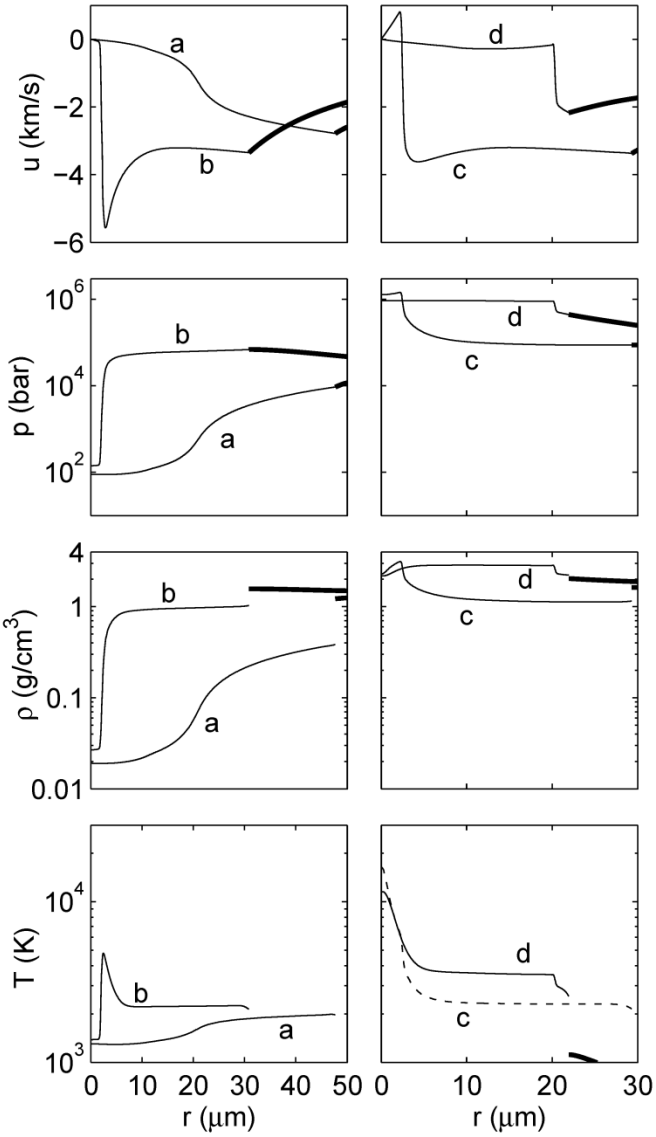

Figure 17. Velocity, pressure, density, and temperature in the bubble interior (thin lines) and exterior liquid (heavy lines) at discrete times corresponding to (a) -8.8, (b) -3.3, (c) -2.9, and (d) -0.47 ns from the moment of minimum radius.

Figure 17 shows the results of the simulation for the bubble interior. Thermodynamic profiles are shown at discrete times chosen to illustrate the interior shock wave (also seen in Figure 16) which mediates the stagnation event. These "snapshots" are taken as the converging compression wave begins to form (a), shortly before it reflects from the bubble center (b), shortly after the reflection (c), and shortly before the shockwave crosses into the liquid, bringing the collapse to a halt.

Several features of this solution are worth noting. First, a well defined shock wave does indeed form inside the bubble. Second, during the transit of the shock wave (a-c), the state inside the bubble is highly non-uniform spatially. However, once the shock enters the liquid (shortly after time d) the state throughout the bubble is quite uniform except for a moderate hot spot at the center. Third, the final, uniform state corresponds to a pressure of about 1 Mbar, density of nearly 3 g/cm^3, and temperature of 3600 K.

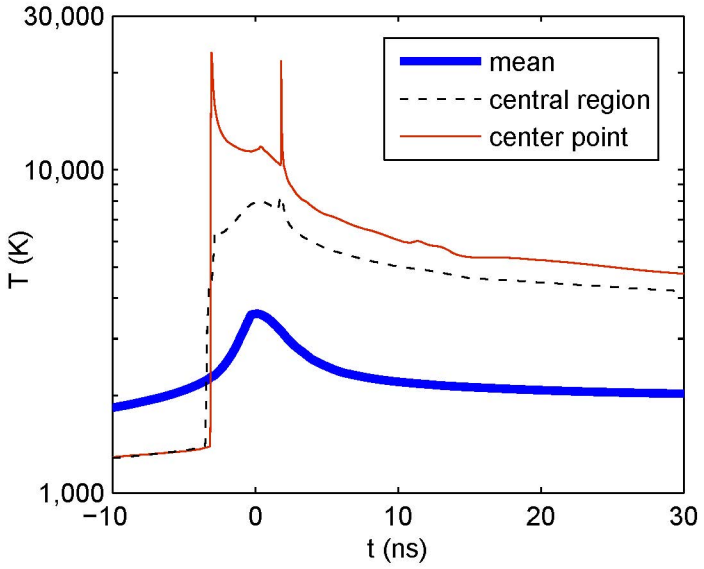

Figure 18. Simulated temperature in the bubble interior, showing the volumetric mean of the entire interior, the central region (10% radius, i.e. 1% projected area and 0.1% of total volume), and the center point.

Note that temperatures above 10,000K are observed only in a small region at the center of the bubble. Figure 18 shows the evolution of the mean temperature in the entire interior compared to the central hot spot. It is interesting that the simulated value at the singular center point is the best match for the experimental data of Figure 14b (which is spatially averaged, and shows that temperature peaks at 13,000 K and exceeds 7,000 K for about 10 ns). On one hand this might be expected since blackbody emissive power scales with T^4. In the simulation at $t = 0$ the center temperature is greater than the mean by a factor of 3.4, yielding 140 times greater intensity. This high temperature region might be expected to overwhelm the low temperature background. However, this reasoning is suspect for two reasons. First, as is made clear in Figure 18, the hot region is less than 1% of the projected area, and 0.1% of the total bubble volume. Second, the spectral power measurements (PMT data reported in Figure 9 and Figure 10) are consistent with blackbody emission at greater than 10,000 K at the full stagnation radius. This conflict currently remains unexplained.

To examine the importance of the equation of state for the bubble interior, the problem was also solved with a simplified vapor state equation in place of the more complete model discussed above. A van der Waals form was chosen, as has often been employed in earlier work[15,20]. In this solution, the stagnation density was smaller by a factor of ~5 and the hot spot temperature peak 2 orders of magnitude higher. This highlights the necessity of a realistic equation of state for the bubble interior.

We also note a related point regarding the modeling of the liquid. In a highly cited study, Wu and Roberts[15] simulated a typical SBSL collapse using the RP equation (24) for the liquid and a van der Waals gas for the interior. This predicted a focusing shock with a temperature peak approaching 10^7 K. We reproduced their results, and then replaced the RP liquid model with the full equations (17-20) employed here, retaining the van der Waals gas interior. This variation produced no interior shocks and a peak

temperature of 8000 K, 3 orders of magnitude lower! This result is presented in its entirety in Appendix A. Clearly, both a reasonable equation of state for the interior and accurate modeling of the liquid compressibility are essential for understanding the stagnation dynamics.

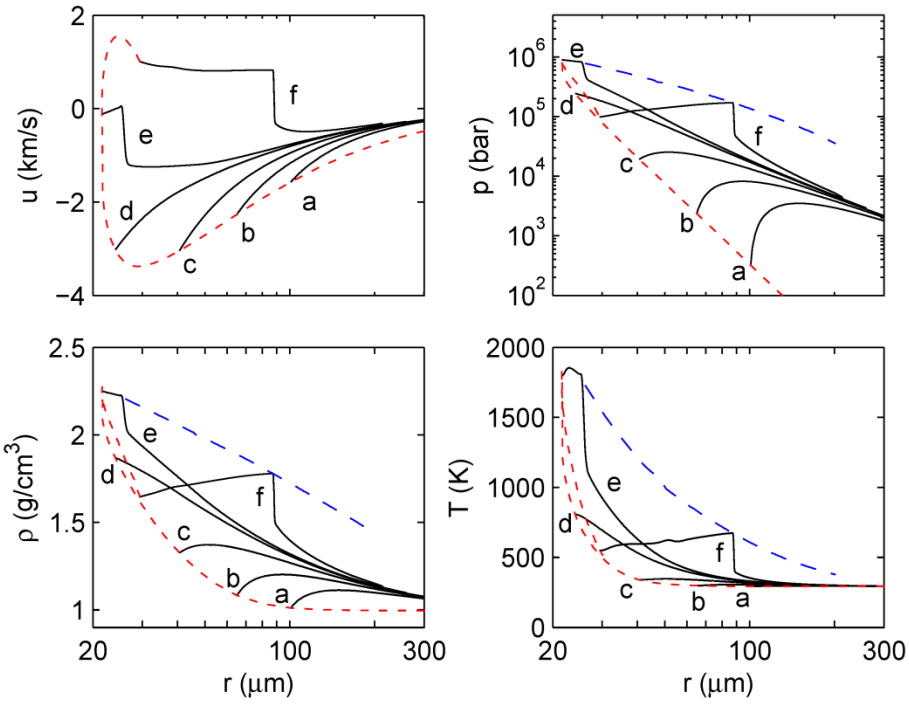

Figure 19. Profiles of velocity, pressure, density, and temperature in the liquid at discrete times corresponding to (a) -35, (b) -16, (c) -6.4, (d) -1.3, (e) 0.0, and (f) 6.5 ns from the moment of minimum radius. Short-dash (red) line is the value at the bubble wall, and long-dash (blue) line is the shock envelope.

Figure 19 shows the simulation results for the liquid with the full model. The liquid in the vicinity of the bubble wall is compressed isentropically to above 100 kbar before being shock compressed to about 1 Mbar. Note that the liquid within a radius of about 100 μm is compressed to greater than 25 kbar before the arrival of the outgoing shock wave. These regions are thus super-cooled with respect to the equilibrium ice VII solid state[63–65] as shown in Figure 20, which gives the equilibrium phase diagram for water in

this regime along with the isentrope for water compressed from STP. It is possible that this phase boundary may be responsible for the irregularity in the shock wave at about 25 ns after stagnation and 130 μm radius observed in all streak data and seen in both panels of Figure 12 (labeled *). Fast homogeneous nucleation might be expected within the smaller ~50 μm radius region in which the pressure exceeds 70 kbar, providing nucleation sites for the adjacent region with pressure in the range of 25-70 kbar. However, there is no direct evidence to support this hypothesis, and it seems equally likely that the dynamic strain due to fluid motion might prevent solidification. This question certainly seems to merit further consideration in future work.

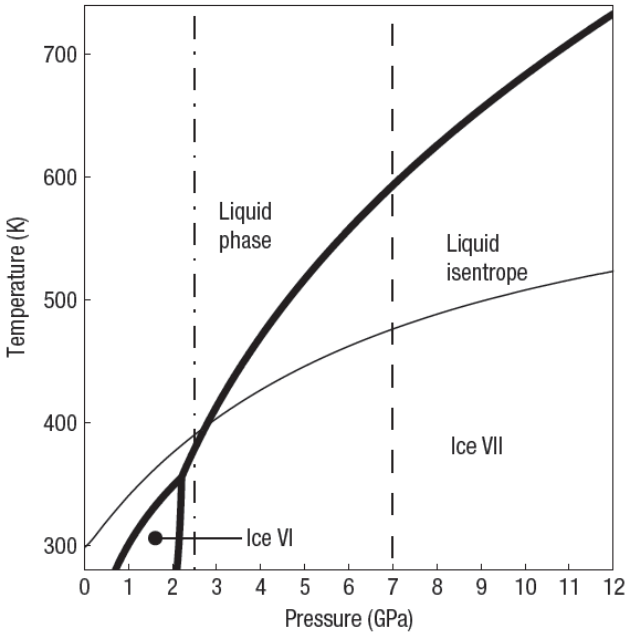

Figure 20. Calculated isentrope for liquid water starting from ambient conditions. The thick lines indicate the known phase boundaries of ice VI and VII. The dash–dot line indicates the lowest pressure observation of heterogeneous freezing whereas the dashed line shows the metastable limit observed in this work [above which homogeneous freezing occurs within a few ns]. Figure and caption from Dolan et. al.[63]

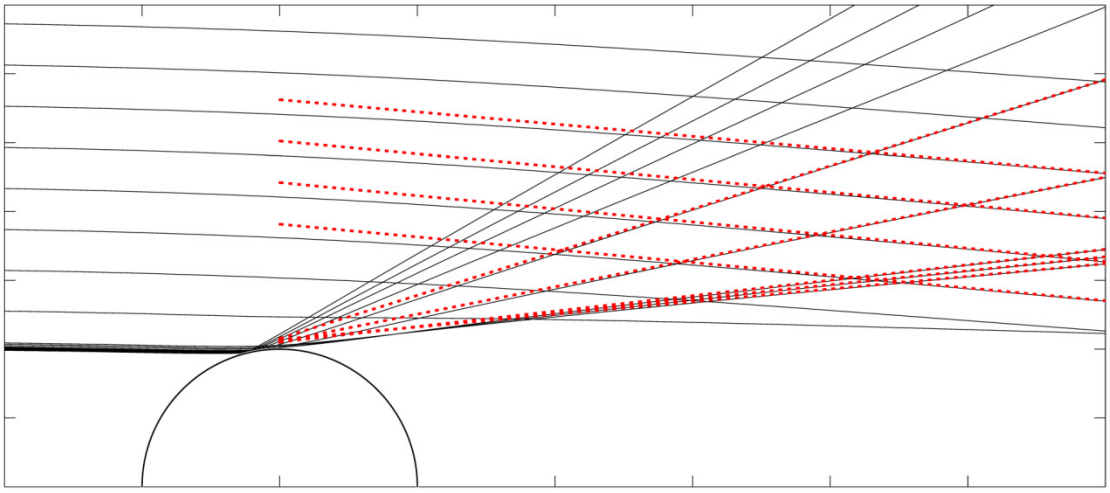

Figure 21. Ray trace showing a few representative rays at a time instant 11 ns prior to the moment of minimum radius. Parallel rays (solid) are incident from the left and refracted by the calculated density profile in the liquid and/or reflected from the bubble surface. Rays which are deflected by 5-20° are projected back to the object plane (heavy red dashed lines) to reconstruct a virtual image.

Finally, we revisit the inferred magnification of the streak image, determined above to be 1.35 by comparison of the experiment with the R vs. t data from the simulation. Now we use the time-resolved density profiles from the simulation to perform a ray tracing analysis and evaluate the plausibility of this magnification assumption. We employ the gradient index ray-tracing algorithm of Sharma[66] and assume that the index of refraction is linear with density as suggested by Zel'dovich[67], i.e. $n = 1 + 0.334\rho$ where ρ has units of g/cm^3. The bubble is illuminated by parallel rays. Rays which are deflected by 5-20° are collected by the objective (as illustrated in Figure 5), so those which meet this criteria are projected back to the object plane to reconstruct the image. Figure 21 shows a typical trace. By repeating this analysis at a range of time instants, the streak image can be virtually reconstructed. This analysis successfully reconstructs both the bubble and the "wings" in the streak image, corresponding to the regions labeled a, b, c, and g in Figure 12a.

This ray tracing analysis shows that the magnification increases from a value of 1.1 to 1.2 during the time frame that the collapsing bubble is visible in Figure 12b. This is somewhat less than the value of 1.35 assumed above. However, the relationship between refractive index of refraction and density employed here is a coarse assumption, which may account for the discrepancy. Nevertheless, this analysis does confirm qualitatively that the magnification is greater than one. In the end, uncertainty of about 20% in the true value of the magnification does remain. This uncertainty directly affects the inferred value of R_{CS}, the radius at which condensation stops, and the resulting quantity of vapor which is trapped in the collapse.

CHAPTER V

CONCLUSIONS AND FUTURE

In the present work I have demonstrated for the first time the production of a directly observable high energy density plasma in a tabletop cavitation collapse device. The stagnation conditions have been quantified with both direct measurements and simulation, which are in reasonable agreement. The maximum energy event drives a 1.8 mm radius vapor bubble in water at 22 bar for a collapse energy of 57 mJ. The stagnation plasma is about 21 μm in diameter with a spatially uniform pressure of 1-3 Mbar, density of about 3 g/cm^3, and temperature of 3500-7000 K. However, a central hot spot reaches temperatures well above 10,000 K. The cold liquid water in the vicinity of the bubble is isentropically compressed to pressures exceeding 100 kbar during the collapse, sub-cooled with respect to the ice VII solid state, and subsequently shock compressed to about 1 Mbar.

This result opens a new opportunity for the study of dynamically compressed materials, high energy density plasmas, and the fundamental dynamics of energetic spherical implosions. It is easy to imagine the introduction of different liquids and gases or even solid particles or surfaces into the event for study at high pressure. However, if accurate state measurements are to be made, further work will be needed to interpret the data with high precision. In particular, uncertainty remains with respect to the optical magnification of the event as viewed through the density gradients of the highly compressed surrounding liquid.

It is important to note that no evidence has been found for production of the extreme temperatures (~10^7 K) predicted in earlier work by others and required to initiate thermonuclear fusion reactions. However, the limits of energy focusing for this type of

event have not yet been reached. If a similar collapse event were conducted in a low vapor pressure liquid such as glycerin, the bubble would contain orders of magnitude less vapor, thus collapsing to smaller radius and dramatically higher energy density. There are practical challenges to such an experiment related to the high viscosity of this liquid, but I believe these are tractable. In a more extreme variant, one might imagine using a needle injected gas bubble in mercury. The high density and acoustic impedance of this liquid would allow dramatic increases in both drive and stagnation pressures. Of course, mercury is opaque and diagnostics would be difficult. However, imaging of gross bubble dynamics might be achieved by GHz ultrasound, and if fusion neutrons were indeed produced, they would easily escape for detection. Such an experiment would be expensive and challenging, and justified only if detailed theory and simulation showed promise.

APPENDIX A

FAILURE OF THE RAYLEIGH-PLESSET MODEL

In SBSL simulation work it has often been assumed[5,15,17,19,20,68,69] that the liquid may be accurately modeled by a modified Rayleigh-Plesset ODE [e.g. equation (24)] which includes a first-order correction for liquid compressibility. Here we show that this assumption fails, and that the Gilmore equation[55], accurate to second-order, is much more accurate.

To address this question, the simulation of Wu and Roberts[15] case (1) was first reproduced precisely. This simulation used equation (24) for the liquid, and a van der Walls equation of state for the bubble interior, and will be referred to as the **RP** solution. Two additional solutions were then calculated for comparison, identical in all respects, except that the liquid was modeled with (i) the Gilmore ODE equation[55], using the Tait state equation (23) for the water (**Gilmore** solution), and (ii) the full Navier-Stokes PDEs, equations (20), (21), and (22), using the same water state equation (**full** solution).

The radius vs. time plots for these three simulations are shown in Figure 22. The first solution matches Wu and Robert's result exactly, showing the collapse brought to a halt by primary and secondary reflected shock waves. The second two solutions show an identical stagnation radius, but do not exhibit shock wave formation. Clearly, the Gilmore solution gives a better approximation of the full solution than does the RP solution.

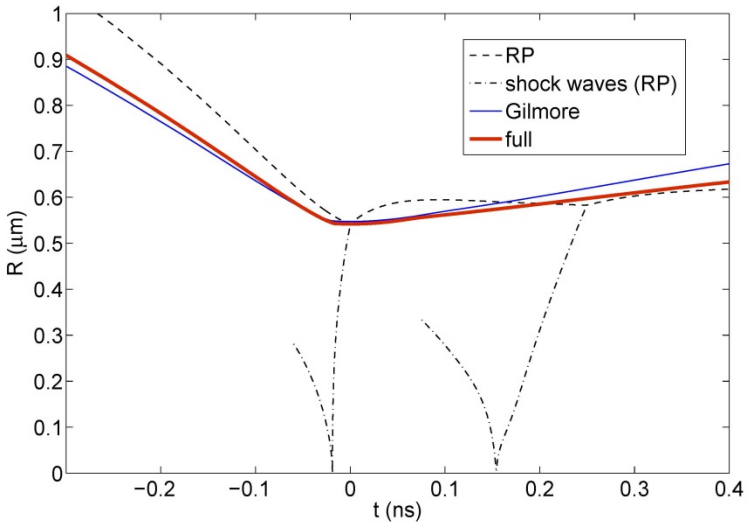

Figure 22. Bubble wall radius vs. time for Wu and Roberts case (1), modeling the liquid with the RP equation (dashed) as in the original work, the Gilmore equation (solid blue), and the full Navier-Stokes equations (heavy red). In the RP case, a converging compression wave which leads the bubble wall steepens into a shock wave (dash-dot) and mediates the stagnation event. The converging compression wave is observed in the other two cases but does not steepen into a shock.

Figure 23 shows the state of the bubble interior in the RP and full solutions shortly after the reflection of the primary converging wave. Note that these two solutions use identical parameters and state equations for the bubble interior, yet the RP solution predicts stagnation pressure which is greater by an order of magnitude and temperature greater by more than two orders of magnitude! How can changing the model for the liquid have so great an effect on the bubble interior?

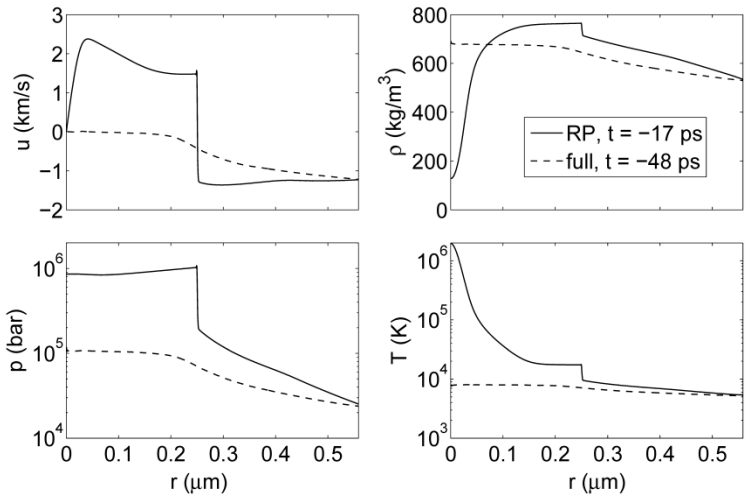

Figure 23. State of the bubble interior after the converging wave has reflected from the bubble center and propagated about half way back to the bubble wall, in the original RP solution (solid) and in the full solution (dashed). The times listed are relative to the instant of minimum bubble radius, which occurs when the wave reaches the bubble wall. Profiles of the velocity (u), density (ρ), pressure (p), and temperature (T) are shown.

The answer to this question is addressed in Figure 24, which shows that the RP solution develops a much higher bubble wall velocity (and acceleration), which clearly promotes the formation of shock waves in the bubble interior. The reason for this is that the first-order approximation of the RP equation accounts for the radiation of acoustic energy into the liquid as a result of pressure changes at the bubble wall (i.e. the energy carried away by the shock wave), but does not account for the kinetic energy converted to enthalpy earlier in the collapse as the liquid is compressed by inertial forces.

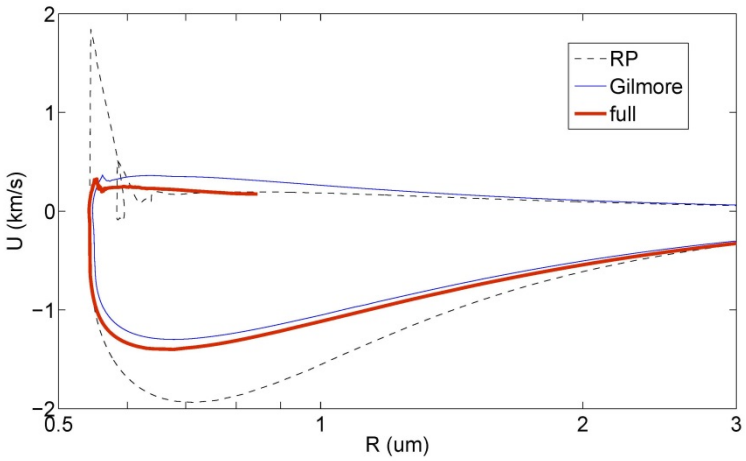

Figure 24. Bubble wall velocity vs. radius for the three different solutions.

The conclusion which can be drawn from this result is that the effects of liquid compressibility must be modeled accurately in order to capture the dynamics of the bubble interior. The Rayleigh-Plesset ODE fails to do so. While the Gilmore equation does give a very good approximation, it seems that the use of the full Navier-Stokes PDEs is justified where practical.

REFERENCES

1. Brennen, C. E. *Cavitation and Bubble Dynamics*. (Oxford University Press: New York, 1995).

2. Rayleigh, L. C. On the pressure developed in a liquid during the collapse of a spherical cavity. *Philosophical Magazine* **34**, 94–98 (1917).

3. Gaitan, D. F. *et al.* Sonoluminescence and bubble dynamics for a single, stable, cavitation bubble. *Journal of the Acoustical Society of America* **91**, 3166–3183 (1992).

4. Barber, B. P., Hiller, R. A., Lofsted, R., Putterman, S. J. & Weninger, K. R. Defining the unknowns of sonoluminescence. *Physics Reports* **281**, 65–143 (1997).

5. Brenner, M. P., Hilgenfeldt, S. & Lohse, D. Single-bubble sonoluminescence. *Reviews of Modern Physics* **74**, 425–484 (2002).

6. Suslick, K. S. & Flannigan, D. J. Inside a collapsing bubble: sonoluminescence and the conditions during cavitation. *Annual Review of Physical Chemistry* **59**, 659–83 (2008).

7. Barber, B. & Putterman, S. Observation of synchronous picosecond sonoluminescence. *Nature* **352**, 318–320 (1991).

8. Gompf, B., Günther, R., Nick, G. & Pecha, R. Resolving sonoluminescence pulse width with time-correlated single photon counting. *Physical Review Letters* **79**, 1405–1408 (1997).

9. Hickling, R. & Plesset, M. S. Collapse and rebound of a spherical bubble in water. *Physics of Fluids* **7**, 7 (1964).

10. Hunter, C. On the collapse of an empty cavity in water. *Journal of Fluid Mechanics* **8**, 241–263 (1960).

11. Holzfuss, J., Rüggeberg, M., Billo, A. & Ruggeberg, M. Shock wave emissions of a sonoluminescing bubble. *Physical Review Letters* **81**, 5434–5437 (1998).

12. Ohl, C.-D., Kurz, T., Geisler, R., Lindau, O. & Lauterborn, W. Bubble dynamics, shock waves and sonoluminescence. *Philosophical Transactions of the Royal Society A* **357**, 269–294 (1999).

13. Weninger, K. R., Evans, P. G. & Putterman, S. J. Time correlated single photon Mie scattering from a sonoluminescing bubble. *Physical Review E* **61**, R1020–R1023 (2000).

14. Pecha, R. & Gompf, B. Microimplosions: cavitation collapse and shock wave emission on a nanosecond time scale. *Physical review letters* **84**, 1328–30 (2000).

15. Wu, C. C. & Roberts, P. H. Shock-wave propagation in a sonoluminescing gas bubble. *Physical review letters* **70**, 3424–3427 (1993).

16. Moss, W. C., Clarke, D. B., White, J. W. & Young, D. A. Hydrodynamic simulations of bubble collapse and picosecond sonoluminescence. *Physics of Fluids* **6**, 2979–2985 (1994).

17. Bass, A., Ruuth, S. J., Camara, C., Merriman, B. & Putterman, S. Molecular dynamics of extreme mass segregation in a rapidly collapsing bubble. *Physical Review Letters* **101**, 234301 (2008).

18. Bosch, H.-S. & Hale, G. M. Improved formulas for fusion cross-sections and thermal reactivities. *Nuclear Fusion* **32**, 611–631 (1992).

19. Lin, H., Storey, B. D. & Szeri, A. J. Inertially driven inhomogeneities in violently collapsing bubbles: the validity of the Rayleigh-Plesset equation. *Journal of Fluid Mechanics* **452**, 145–162 (2002).

20. An, Y. & Ying, C. Model of single bubble sonoluminescence. *Physical Review E* **71**, 036308 (2005).

21. Hiller, R., Putterman, S. J. & Barber, B. P. Spectrum of synchronous picosecond sonoluminescence. *Physical Review Letters* **69**, 1182–1184 (1992).

22. Vazquez, G., Camara, C., Putterman, S. & Weninger, K. Sonoluminescence: nature's smallest blackbody. *Optics Letters* **26**, 575–577 (2001).

23. Hammer, D. & Frommhold, L. Topical review Sonoluminescence : how bubbles glow. *Journal of Modern Optics* **48**, 239–277 (2001).

24. Hopkins, S. D., Putterman, S. J., Kappus, B. A., Suslick, K. S. & Camara, C. G. Dynamics of a sonoluminescing bubble in sulfuric acid. *Physical Review Letters* **95**, 254301 (2005).

25. Flannigan, D. J., Hopkins, S. D., Camara, C. G., Putterman, S. J. & Suslick, K. S. Measurement of pressure and density inside a single sonoluminescing bubble. *Physical Review Letters* **96**, 204301 (2006).

26. Camara, C., Putterman, S. & Kirilov, E. Sonoluminescence from a single bubble driven at 1 megahertz. *Physical Review Letters* **92**, 124301 (2004).

27. Flannigan, D. J. & Suslick, K. S. Plasma formation and temperature measurement during single-bubble cavitation. *Nature* **434**, 52–55 (2005).

28. Flannigan, D. J. & Suslick, K. S. Plasma line emission during single-bubble cavitation. *Physical Review Letters* **95**, 044301 (2005).

29. Flannigan, D. J. & Suslick, K. S. Inertially confined plasma in an imploding bubble. *Nature Physics* **6**, 598–601 (2010).

30. Thomas, J.-L. L., Forterre, Y. & Fink, M. Boosting sonoluminescence with a high-intensity ultrasonic pulse focused on the bubble by an adaptive array. *Physical Review Letters* **88**, 74302 (2002).

31. Thomas, J.-L. Inhomogeneous pressure field inside a collapsing bubble accelerated by an acoustic pulse. *Physical Review E* **70**, 016305 (2004).

32. Holzfuss, J., Rüggeberg, M. & Mettin, R. Boosting sonoluminescence. *Physical Review Letters* **81**, 1961–1964 (1998).

33. Hargreaves, K. & Matula, T. J. The radial motion of a sonoluminescence bubble driven with multiple harmonics. *Journal of the Acoustical Society of America* **107**, 1774–1776 (2000).

34. Krefting, D., Mettin, R. & Lauterborn, W. Two-frequency driven single-bubble sonoluminescence. *Journal of the Acoustical Society of America* **112**, 1918–1927 (2002).

35. Lu, X. Z., Prosperetti, A., Toegel, R. & Lohse, D. Harmonic enhancement of single-bubble sonoluminescence. *Physical Review E* **67**, 056310 (2003).

36. Urteaga, R. & Bonetto, F. J. Trapping an intensely bright, stable sonoluminescing bubble. *Physical Review Letters* **100**, 074302 (2008).

37. Chakravarty, A., Georghiou, T., Phillipson, T. E. & Walton, A. J. Stable sonoluminescence within a water hammer tube. *Physical Review E* **69**, 066317 (2004).

38. Su, C. K., Camara, C., Kappus, B. & Putterman, S. J. Cavitation luminescence in a water hammer: Upscaling sonoluminescence. *Physics of Fluids* **15**, 1457–1461 (2003).

39. Urteaga, R., Garcia-Martinez, P. L., Bonetto, F. J. & García-Martínez, P. Dynamics of sonoluminescing bubbles within a liquid hammer device. *Physical Review E* **79**, 016306 (2009).

40. Gaitan, D. F. *et al.* Transient cavitation in high-quality-factor resonators at high static pressures. *The Journal of the Acoustical Society of America* **127**, 3456–3465 (2010).

41. Kurz, T., Kröninger, D., Geisler, R. & Lauterborn, W. Optic cavitation in an ultrasonic field. *Physical Review E* **74**, 066307 (2006).

42. Lauterborn, W. & Kurz, T. Physics of bubble oscillations. *Reports on Progress in Physics* **73**, 106501 (2010).

43. Kappus, B., Khalid, S., Chakravarty, A. & Putterman, S. Phase transition to an opaque plasma in a sonoluminescing bubble. *Physical Review Letters* **106**, 234302 (2011).

44. Ohl, C. D., Lindau, O. & Lauterborn, W. Luminescence from spherically and aspherically collapsing laser induced bubbles. *Physical Review Letters* **80**, 393–396 (1998).

45. Baghdassarian, O., Tabbert, B. & Williams, G. A. Luminescence characteristics of laser-induced bubbles in water. *Physical Review Letters* **83**, 2437–2440 (1999).

46. Baghdassarian, O., Chu, H. C., Tabbert, B. & Williams, G. A. Spectrum of luminescence from laser-created bubbles in water. *Physical Review Letters* **86**, 4934–4937 (2001).

47. Ohl, C. D. Probing luminescence from nonspherical bubble collapse. *Physics of fluids* **14**, 2700–2708 (2002).

48. Brujan, E. A., Hecht, D. S., Lee, F. & Williams, G. A. Properties of luminescence from laser-created bubbles in pressurized water. *Physical Review E* **72**, 066310 (2005).

49. Drake, R. P. *High Energy Density Physics*. (Springer: New York, 2006).

50. Moss, W. C., Clarke, D. B., White, J. W. & Young, D. A. Sonoluminescence and the prospects for table-top micro-thermonuclear fusion. *Physics Letters A* **211**, 69–74 (1996).

51. Jones, A. H., Isbell, W. M. & Maiden, C. J. Measurement of very-high-pressure properties of materials using a light-gas gun. *Journal of Applied Physics* **37**, 3493–3499 (1966).

52. Soures, J. M. *et al.* Direct-drive laser-fusion experiments with the OMEGA, 60-beam, >40 kJ, ultraviolet laser system. *Physics of Plasmas* **3**, 2108–2112 (1996).

53. Matzen, M. K. *et al.* Pulsed-power-driven high energy density physics and inertial confinement fusion research. *Physics of Plasmas* **12**, 055503 (2005).

54. Ramsey, M. C. & Pitz, R. W. Energetic cavitation collapse generates 3 . 2 Mbar plasma with a 1 . 4 J driver. *Physical Review Letters* **110**, 154301 (2013).

55. Gilmore, F. R. The growth or collapse of a spherical bubble in a viscous compressible liquid. *Office of Naval Research* **26-4**, 1–40 (1952).

56. Vogel, A., Nahen, K., Theisen, D. & Noack, J. Plasma formation in water by picosecond and nanosecond Nd:YAC laser pulses .1. Optical breakdown at

threshold and superthreshold irradiance. *IEEE Journal of Selected Topics in Quantum Electronics* **2**, 847–860 (1996).

57. Temkin, S. *Elements of Acoustics*. (Wiley: New York, 1981).

58. Storey, B. D. & Szeri, A. J. Water vapour, sonoluminescence and sonochemistry. *Proceedings of the Royal Society of London A* **456**, 1685–1709 (2000).

59. Ree, F. H. *SESAME 7150, in Lawrence Livermore National Laboratory Report UCRL-52190*. (1978).

60. Keller, J. B. & Kolodner, I. I. Damping of underwater explosion bubble oscillations. *Journal of Applied Physics* **27**, 1152–1161 (1956).

61. Keller, J. B. & Miksis, M. Bubble oscillations of large amplitude. *Journal of the Acoustical Society of America* **68**, 628–633 (1980).

62. Prosperetti, A. & Lezzi, A. Bubble dynamics in a compressible liquid. Part 1. First-order theory. *Journal of Fluid Mechanics* **168**, 457–478 (1986).

63. Dolan, D. H., Knudson, M. D., Hall, C. A. & Deeney, C. A metastable limit for compressed liquid water. *Nature Physics* **3**, 339–342 (2007).

64. Dolan, D. H. & Gupta, Y. M. Nanosecond freezing of water under multiple shock wave compression: optical transmission and imaging measurements. *The Journal of chemical physics* **121**, 9050–9057 (2004).

65. Hickling, R. Nucleation of freezing by cavity collapse and its relation to cavitation damage. *Nature* **4987**, 915–917 (1965).

66. Sakamoto, T. Ray trace algorithms for GRIN media. *Applied optics* **26**, 2943–2946 (1987).

67. Zel'dovich, Y. B. & Raizer, Y. P. *Physics of Shock Waves and High-Temperature Hydrodynamic Phenomena*. 916 (Dover: Mineola, New York, 1966).

68. Vuong, V. Q., Szeri, A. J. & Young, D. A. Shock formation within sonoluminescence bubbles. *Physics of Fluids* **11**, 10–17 (1999).

69. Yuan, L., Cheng, H., Chu, M.-C. & Leung, P. Physical parameters affecting sonoluminescence: A self-consistent hydrodynamic study. *Physical Review E* **57**, 4265–4280 (1998).